INSTITUTE FOR FUSION STUDIES

DOE/ET/53088-445 IFSR #445

Numerical Simulation of Ion Temperature Gradient Driven Modes in the Presence of Ion-Ion Collisions

X. Q. Xu
Institute for Fusion Studies
The University of Texas at Austin
Austin, Texas 78712

M. N. Rosenbluth
Department of Physics
University of California, San Diego
La Jolla, California 92093
and
General Atomics
San Diego, California 92138

August 1990

THE UNIVERSITY OF TEXAS

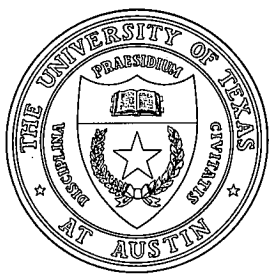

AUSTIN

Numerical Simulation of Ion Temperature Gradient Driven Modes in the Presence of Ion-Ion Collisions

X. Q. Xu

Institute for Fusion Studies, Univ. of Texas at Austin

M. N. Rosenbluth

Dept. of Phys., Univ. of Calif., San Diego

and

General Atomics

Abstract

Ion temperature gradient driven modes in the presence of ion-ion collisions in a toroidal geometry with trapped ions have been studied by using a $1\frac{2}{2}d$ linearized gyro-kinetic particle simulation code in the electrostatic limit. The purpose of the investigation is to try to understand the physics of flat density discharges, in order to test the marginal stability hypothesis. Results giving threshold conditions of L_{Ti}/R_0, an upper bound on k_χ, and linear growth rates and mode frequencies over all wavelengths for the collisionless ion temperature gradient driven modes are obtained. The behavior of ion temperature gradient driven instabilities in the transition from slab to toroidal geometry, with trapped ions, is shown. A Monte-Carlo scheme for the inclusion of ion-ion collisions, in which ions can undergo Coulomb collisional dynamical friction, velocity space diffusion and random walk of guiding centers, has been constructed. The effects of ion-ion collisions on the long wave length limit of the ion modes is discussed.

I. Introduction

Recent experimental results from a number of tokamaks such as DIII-D and JET have indicated that the electron density profile in H-mode discharges can be nearly flat over most of the plasma.[1-6] The conditions have very interesting implications for pictures of anomalous thermal transport based on the presence of ion temperature gradient (ITG or ∇T_i) drift instabilities.[7] Most of the theoretical analyses of this instability have considered the various wavelength limit cases, such as long-wavelength trapped ion modes, toroidal branch ∇T_i modes, and slab-like ∇T_i modes.[7-13,42] Small parameters invoked in theoretical analyses are in reality often of order unity. The present work provides a full kinetic description of the ∇T_i-mode in the presence of ion-ion collisions over all wavelengths, and demonstrates the transition from one mode to another under certain conditions. This is an important issue because the real experiments in tokamaks are not in the extreme model conditions of previous theory. From the quantitative comparison between theoretical calculation and experimental observations one can gain confidence in understanding the mechanisms of the observed anomalous thermal transport in the H-mode cases.

The stability threshold condition of the ∇T_i-mode in the flat density profile limit has received considerable attention recently[7-12,14,15] because of its possible importance in mechanisms of anomalous energy transport in tokamak H-mode discharges. Various theoretical and experimental studies have argued that a large diffusion coefficient should provide a local flattening of the ion temperature profile until the mode reaches an almost marginally stable situation.[16] The relevant stability parameter governing these modes is characterized by a critical temperature gradient; for the slab modes, one obtains a critical value of L_{Ti}/L_s (L_{Ti} is the ion temperature gradient length and L_s is the shear length), whereas for the toroidal mode, a critical L_{Ti}/R_0 (R_0 is the major radius) is obtained. Observed values of L_{Ti}/R_0 for stable profiles from DIII-D[14] exhibit a lower bound of the order 0.1, somewhat smaller than the expected stability boundary for toroidal ITG modes based on the various kinetic models.[7-12] In addition, to test and confirm the ion temperature gradient driven turbulence (ITGDT) marginal stability of the tokamak plasma, the TFTR group has conducted perturbed experiments in L-mode,[15] in which the peaked density profiles of supershots have been transiently broadened using either a helium gas

puff or a deuterium pellet. The consequences of the different perturbations are the same: the plasma is driven far from the theoretical ITG stability boundary during the perturbation, but the ion heat flux remains unchanged. Doubt regarding the contribution of ITG modes to the ion thermal transport has therefore been raised.[14,15] The uncertainty regarding this question affects both the interpretation of the experimental results on the ion thermal transport in tokamaks and the theory of anomalous transport associated with the ∇T_i driven microinstabilities. Obviously, for such a situation a careful evaluation of the stability threshold is indeed needed. In order to properly treat the regime near the critical value of L_{Ti}/R_0, we provide full kinetic calculations of the ∇T_i driven instability in order to obtain a realistic value of the threshold as a function of various relevant parameters.

Ion temperature gradient driven modes in the presence of ion-ion collisions in a toroidal geometry with trapped ions have been studied by using a $1\frac{2}{2}d$ linearized gyro-kinetic particle simulation code. The code is developed in the ballooning representation with a new particle δf algorithm,[17] which integrates the ion electrostatic gyro-kinetic equation along particle trajectories. The ballooning mode representation is employed to reduce the system to a one dimensional spatial problem in the extended poloidal angle variable.[18,19] Complete trapped and circulating ion dynamics are included in this analysis, which is valid for arbitrary mode frequencies compared to the particle bounce or transit frequency and ion-ion collision frequency, and also for arbitrary perpendicular wavelength compared to the particle gyroradius or banana width. Hence, all forms of resonances among bounce, transit and magnetic drift frequencies as well as ion-ion collisional dissipation are taken into account here without approximations. As the density gradient is flattened, the dominant electrostatic microinstability in toroidal systems is an ion mode driven by the interchange and ∇T_i-destabilizing mechanisms, with the nonadiabatic trapped electron dynamics making negligible contributions.[7] Thus in this work we retain only the adiabatic electron response. While our method is easily generalizable to arbitrary geometry, we have so far only made detailed calculations for unshifted circular equilibria.

The low frequency long-wavelength trapped-ion mode was discovered by Kadomtsev and Pogutse in the banana regime.[20] Such a potentially dangerous unstable mode is relevant for transport studies because modes at the long wavelength limit are expected to

produce larger transport than at the short one. Thus much subsequent research in the past decades has been directed towards achieving a better understanding of the stability criteria and the possible effects of such modes on plasma confinement.[21-27] With regard to analyzing the stabilizing effect of ion-ion collisions on ion temperature gradient driven trapped particle modes, Xu and Rosenbluth[27] have used a variational method with the Lorentz collision operator to obtain a stability threshold condition for the mode in the radially local limit. In this approximation the perturbed potential was assumed to have a moderately ballooning structure in the outer part of the torus, which can be destabilized by the combined effects of the trapped ion temperature gradient and the local unfavorable curvature with adiabatic electron and circulating ion responses. Thus to address this issue more accurately it is important to develop a more sophisticated numerical Coulomb collision operator. The analysis presented in this paper accounts for the full dissipative kinetic influence of ion dynamics on the trapped ion modes and toroidal branch of ∇T_i modes with the use of a linearized Fokker-Planck collision operator.

The paper is organized as follows. In Sec. II. a general equation is derived for the electrostatic potential when nonadiabatic electron dynamics are neglected. The numerical techniques employed to generate gyro-kinetic particle simulations are described in Sec. III. A comparison between theory and simulation results from a linearized electrostatic $1\frac{2}{2}d$ gyro-kinetic particle code in a sheared slab geometry is given in Sec. IV. In Sec. V. we present our full kinetic calculation for a toroidal geometry. The results are compared with those obtained from two different realistic Tokamak discharges: H-mode in DIII-D, Hot-ion H-mode ($T_i > T_e$) in DIII-D. Finally, conclusions are discussed in Sec. VI. and the new Monte-Carlo collision scheme employed is derived in detail in Appendix.

II. General Formalism

The low beta toroidal geometry linearized gyro-kinetic Vlasov equation written in the ballooning representation[28,29] is

$$(\frac{\partial}{\partial t} + v_{\parallel}\frac{\partial}{\partial l} + i\omega_{dj})h_j(l) = (\frac{\partial}{\partial t} + i\omega_{*j}^T)\frac{q_j}{T_j}F_{mj}J_0\phi + < e^{iL}C(h_j)e^{-iL} >, \quad (1)$$

where we have included the finite Larmor radius effects through the usual zero-order Bessel function $J_0 = J_0(k_\perp \rho_j)$. The quantity $< e^{iL}C(h_j)e^{-iL} >$ represents the gyro-averaged Fokker-Planck collision operator, which we discuss in detail below, and l is the arc length along a field line.

The perturbed distribution function $\tilde{f}$ is given by

$$\tilde{f} = f\exp[inS(r,\chi,\zeta) - i\omega t], \quad (2)$$

where

$$f(l) = -\frac{q_j\phi(l)}{T_j}F_{mj} + h_j(l), \quad (3)$$

with S being the usual eikonal ($\vec{k}_\perp = \nabla S$), r the minor radius, $\chi \equiv l/(qR)$ the poloidal angle and ζ the toroidal angle. The distribution function F_{mj} is assumed to be Maxwellian for jth species, and h_j is the nonadiabatic portion of the perturbed distribution function.

Here we list below the definitions of the terms which appear in Eqs. (1) -(3).

$$\begin{aligned}
\omega_{*j}^T &= \frac{cT_j\vec{k}\times\vec{b}\cdot\nabla F_{mj}}{q_jBF_{mj}} = \omega_{*j}\left[1 + \eta_j(\frac{E}{T_j} - \frac{3}{2})\right], \\
\omega_{dj} &= \hat{\omega}_{kj}(2E - \mu B)/T_j, \hat{\omega}_{kj} = \frac{cT_j}{q_jB}\left(\vec{\kappa}\times\vec{b}\cdot\vec{k}\right), \\
\vec{\kappa} &= (\vec{b}\cdot\nabla\vec{b}), \\
\mu &= \frac{m_jv_\perp^2}{2B^2}, \\
E &= \frac{m_jv^2}{2},
\end{aligned} \quad (4)$$

$\omega_{*j} = -k_\chi\rho_j v_{thj}/(L_{nj})$ is the diamagnetic drift frequency, $\rho_j = v_{thj}/\Omega_{cj}$ the Larmor radius, $v_{thj} = \sqrt{(T_j/m_j)}$ the thermal speed, $\Omega_{cj} = q_jB/(m_jc)$ the cyclotron frequency, $L_{nj} = -(d\ln n_j/dr)^{-1}$ the density gradient scale length, $k_\chi = -m/r$ the poloidal wave

vector, and $\eta_j = L_{nj}/L_{Tj}$ with L_{Tj} the temperature gradient scale length. For the model MHD equilibrium,[19] we then have

$$\begin{aligned}
\vec{k_\perp} &= n\nabla S = -k_\chi[\vec{e}_\chi + \hat{s}(\chi-\chi_0)\vec{e}_r], \\
\vec{b}\times\vec{\kappa}\cdot\vec{k} &= \frac{k_\chi}{R_0}[\cos\chi + \hat{s}(\chi-\chi_0)\sin\chi], \\
\frac{\partial}{\partial l} &= (\vec{b}\cdot\nabla\chi)\frac{\partial}{\partial\chi} = \frac{1}{R_0 q}\frac{\partial}{\partial\chi},
\end{aligned} \tag{4a}$$

where $\hat{s} \equiv d\ln q/d\ln r$ measures the average shear and χ_0 is the parameter in the ballooning hierarchy.

Since detrapping due to ion-ion collisions can result in stabilizing contributions to low frequency and long wave-length trapped ion instabilities,[27] it is desirable to use as complete an ion-ion collision operator as possible. To this end, the ion-ion Fokker-Planck collision operator is derived by employing the gyro-kinetic formalism summarized in Eq. (A.28) in Appendix, and can be written as

$$\begin{aligned}
< e^{iL}C(h_j)e^{-iL} > &= \frac{\partial}{\partial v_\perp^2}\left(\nu_{s\perp}(v_\perp^2,v)v^2 h_j\right) + \frac{\partial}{\partial v_\parallel}\left(\nu_{s\parallel}(v)v_\parallel h_j\right) \\
&+ \frac{1}{2}\frac{\partial^2}{(\partial v_\perp^2)^2}\left(\nu_\perp(v_\perp^2,v)v^4 h_j\right) + \frac{1}{2}\frac{\partial^2}{\partial v_\parallel^2}\left(\nu_\parallel(v_\parallel^2,v)v^2 h_j\right) \\
&+ \frac{\partial^2}{\partial v_\perp^2\partial v_\parallel}\left(\nu_{\parallel\perp}(v_\parallel,v_\perp)v^3 h_j\right) - \frac{k_\perp^2}{2\Omega_{cj}^2}(2G + \frac{v_\perp^2}{v^2}H)h_j \\
&+ \frac{F_{mj}}{n_0 v_{Tj}^2}\left(v_\parallel J_0\int d^3v v_\parallel J_0 F h_j + v_\perp J_1\int d^3v v_\perp J_1 F h_j\right) \\
&+ (\frac{v^2}{2v_{Tj}^2} - \frac{3}{2})\frac{2F_{mj}}{3n_0 v_{Tj}^2}J_0\int d^3v(v^2F - 3G - H)J_0 h_j.
\end{aligned} \tag{5}$$

The definitions of the terms which appear in Eq. (5) are given in Eqs. (A.17a) and (A.22)-(A.26) in Appendix. Looking at Eq. (5) we see that the first two terms represent the dynamical friction required to relax the test particles' velocity to the centroid of the velocity distribution of the Maxwellian background particles, that the next three terms give the velocity space diffusion causing the velocity distribution of the test particles to maintain a thermal spread comparable to that of the background particles, and that the sixth term drives the classical diffusion due to the random walk of particle guiding centers. The last two terms are the sources needed to conserve the energy and momentum of the system.

Since it is not convenient numerically to retain terms involving $\partial\phi/\partial t$, Eq. (1) may be rewritten by defining

$$h_j = \frac{q_j F_{mj}\phi}{T_j} J_0 + g_j, \tag{6}$$

to obtain

$$\begin{aligned}
[\frac{d}{dt} + i\omega_{dj} + \frac{k_\perp^2}{2\Omega_{cj}^2}(2G + \frac{v_\perp^2}{v^2}H)]g_j(l) = \{&i(\omega_*^T - \omega_{dj}) - \frac{k_\perp^2}{2\Omega_{cj}^2}(2G + \frac{v_\perp^2}{v^2}H) \\
&- [\nu_{s\perp}(v_\perp^2, v)v^2 \frac{J_1}{J_0}\frac{k_\perp}{2\Omega_{cj}v_\perp} + \nu_\perp(v_\perp^2, v)v^4(\frac{k_\perp}{2\sqrt{2}\Omega_{cj}v_\perp})^2]\}\frac{q_j}{T_j}F_{mj}J_0\phi \\
&- v_\parallel \frac{\partial}{\partial l}(J_0\phi)\frac{q_j}{T_j}F_{mj} \\
&+ \frac{F_m}{n_0 v_T^2}\left(v_\parallel J_0 \int d^3v v_\parallel J_0 F h_j + v_\perp J_1 \int d^3v v_\perp J_1 F h_j\right) \\
&+ (\frac{v^2}{2v_T^2} - \frac{3}{2})\frac{2F_M}{3n_0 v_T^2} J_0 \int d^3v (v^2 F - 3G - H) J_0 h_j.
\end{aligned} \tag{7}$$

The operator

$$\begin{aligned}
\frac{d}{dt}g_j = (\frac{\partial}{\partial t} + v_\parallel\frac{\partial}{\partial l})g_j &- \frac{\partial}{\partial v_\perp^2}\left(\nu_{s\perp}(v_\perp^2, v)v^2 g_j\right) - \frac{\partial}{\partial v_\parallel}\left(\nu_{s\parallel}(v)v_\parallel g_j\right) \\
&- \frac{1}{2}\frac{\partial^2}{(\partial v_\perp^2)^2}\left(\nu_\perp(v_\perp^2, v)v^4 g_j\right) - \frac{1}{2}\frac{\partial^2}{\partial v_\parallel^2}\left(\nu_\parallel(v_\parallel^2, v)v^2 g_j\right) \\
&- \frac{\partial^2}{\partial v_\perp^2 \partial v_\parallel}\left(\nu_{\parallel\perp}(v_\parallel, v_\perp)v^3 g_j\right)
\end{aligned} \tag{8}$$

represents how the individual motion of the charged particles is subject to the action of magnetic fields and also random walk arising from collisions with a plasma whose components have Maxwellian distributions.

Upon introducing the integrating factor along the particle orbit,

$$\beta = \int_{t_0}^{t} dt'[\omega_{dj}(t') + \frac{k_\perp^2}{2\Omega_{cj}^2}(2G + \frac{v_\perp^2}{v^2}H)] = \overline{\beta} + \omega_{*j}\frac{\hat{S}L_n}{\varepsilon R_0}[v_\parallel(l - l_0) - v_\parallel(t_0)(l(t_0) - l_0)], \tag{9}$$

where

$$\overline{\beta} = 0.5\frac{L_n}{R_0}\int_{t_0}^{t} dt'\omega_{*j}\left[(v^2 + v_\parallel^2)\cos(l/qR_0) + \frac{2\hat{S}v_\parallel^2}{\varepsilon} + \frac{k_\perp^2}{2\Omega_{cj}^2}(2G + \frac{v_\perp^2}{v^2}H)\right],$$

and setting

$$g = \overline{g} e^{-i\beta}, \tag{10}$$

the following equation for g_j is obtained:

$$\begin{aligned}
\frac{d}{dt}\overline{g}_j(l) = \{ & i(\omega_{*j}^T - \omega_{dj}) - \frac{k_\perp^2}{2\Omega_{cj}^2}(2G + \frac{v_\perp^2}{v^2}H) \\
& - [\nu_{s\perp}(v_\perp^2, v)v^2 \frac{J_1}{J_0}\frac{k_\perp}{2\Omega_{cj}v_\perp} + \nu_\perp(v_\perp^2, v)v^4(\frac{k_\perp}{2\sqrt{2}\Omega_{cj}v_\perp})^2]\} \frac{q_j}{T_j} F_{mj} J_0 \phi e^{i\beta} \\
& - v_\parallel \frac{\partial}{\partial l}(J_0\phi(l))\frac{q_j}{T_j}F_{mj}e^{i\beta} \\
& + \frac{F_{mj}}{n_0 v_T^2}e^{i\beta}\left(v_\parallel J_0 \int d^3v v_\parallel J_0 F h_j + v_\perp J_1 \int d^3v v_\perp J_1 F h_j\right) \\
& + (\frac{v^2}{2v_T^2} - \frac{3}{2})\frac{2F_{mj}}{3n_0 v_T^2} J_0 e^{i\beta} \int d^3v (v^2 F - 3G - H) J_0 h_j.
\end{aligned} \tag{11}$$

The perturbed ion density response is

$$\tilde{n}_i(l) = -\frac{n_0 q_i \phi}{T_i}(1 - I_0(b_i)e^{-b_i}) + \int d^3v \overline{g}_i J_0 e^{-i\beta},$$

where $b_i = k_\perp^2 \rho_i^2$.

By assuming an adiabatic electron response the dynamics of a low-frequency electrostatic perturbation is described by the quasi-neutrality condition

$$\phi = (1 + 1/\tau - I_0(b_i)e^{-b_i})^{-1} \int d^3v \overline{g}_i J_0 e^{-i\beta} n_0 \frac{T_i}{n_0 q_i}. \tag{12}$$

The complete set of equations (11) and (12) determine the basic form of the low-frequency ion mode problem. Our theoretical investigations of these modes will be done based on a numerical particle simulation technique. The advantage of this Monte-Carlo approach is the better sampling of phase space as well as inclusion of ion-ion Coulumb collisions with less approximations as compared to solving the time dependent gyro-kinetic equations either directly or by eigenmode analysis.

III. Numerical Techniques

In this section, we will discuss the numerical schemes for solving the gyro-kinetic equation (11) and quasineutrality condition (12) based on the δf algorithm.[17] A simple δf numerical particle algorithm which we will study below can be outlined as follows. The system is described by N particles with coordinate l and velocity $(v_\parallel, v_\perp)$ which evolve according to the equation of motion Eq. (13), which is suitably time differenced. The perturbed distribution function $\overline{g}_i$ in Eq. (11) is computed by integrating source terms along the particle trajectory given by Eq. (13). The fields ϕ are obtained from $\overline{g}$ on a grid by accumulating particles to nearby gridpoints using various weightings, instead directly computing integrals of $\overline{g}$ over some regions of phase space in Eq. (12). This technique can greatly reduce noise and/or particle requirements for investigating the ion temperature driven mode, since equilibrium thermal noise is eliminated as g_i is much smaller than the Maxwellian background distribution F_{mi}.

As we know from Eq. (8), an individual particle undergoes Brownian motion: the permanent motion of these particles is maintained by fluctuations of their velocities during collisions. The phenomenological description of Brownian motion in the framework of individual particle description can be obtained as follows. Between two collisions the particle moves along the particle orbit which is determined by the external magnetic fields. Therefore energy v^2 and magnetic moment μ of the particles are conserved. Considering for simplicity a toroidal geometry with circular magnetic surface equilibria, the unperturbed magnetic field strength may be written as $B(l) = B_0/(1 + \varepsilon \cos\chi)$, with $\varepsilon = r/R_0$, where R_0 is the major radius at the center of the magnetic surface. Thus the equations of the particle orbits between two collisions are given by

$$\begin{aligned} \frac{dl}{dt} &= v_\parallel(l), l = qR_0\chi \\ v_\parallel(l) &= (v^2 - 2\mu B(l)/m_i)^{1/2}. \end{aligned} \tag{13}$$

We indicate by $r = r^{(0)}$ the magnetic surface on which a guiding center orbit is centered so that

$$r(t) - r^{(0)} = \frac{q(v_\parallel - v_\parallel^{(0)})}{\varepsilon v_T}\rho_i.$$

Meanwhile the particle orbit will be changed by the Coulomb collision. To develop formulae for a probabilistic numerical approach for the inclusion of Coulomb collisions, we examine the collisional evolution of the velocity of a test particle for short times $\Delta t \gg \delta t$ (for validity of the dynamic friction and velocity diffusion coefficients) where the velocity changes are small. By assuming a scattering in which $\Delta v_\parallel$ and $\Delta v_\perp^2 - \beta \Delta v_\parallel$ have square probability amplitudes, from Eq. (8) we find that the new velocities $v_\parallel'$ and $v_\perp'^2$ can be evaluated from the old velocities ($v_\parallel$, $v_\perp^2$,v) by (see Eq. (A.36) in Appendix)

$$v_\parallel' = v_\parallel[1 - \nu_{s\parallel}(v)\Delta t] + 2\sqrt{3}(R_{s1} - 0.5)\sqrt{\nu_\parallel(v_\parallel^2, v)v^2\Delta t}$$

$$v_\perp'^2 = v_\perp^2 - v^2\nu_{s\perp}(v_\perp^2, v)\Delta t + 2\sqrt{3}(R_{s2} - 0.5)v^2\sqrt{[\nu_\perp(v_\perp^2, v) - \frac{\nu_\perp(v_\parallel, v_\perp^2)}{\nu_\parallel(v_\parallel^2, v)}]\Delta t}$$

$$+ 2\sqrt{3}(R_{s1} - 0.5)v^2\sqrt{\nu_\parallel(v_\parallel^2, v)\Delta t} \qquad (14)$$

where R_{s1} and R_{s2} are two independent random variables which are evenly distributed between 0 and 1. This provides a Monte-Carlo algorithm for advancing the velocities $v_\parallel$ and $v_\perp^2$ taking into account the Coulomb collisional dynamical friction and velocity space diffusion occuring over the short time Δt, where Δt is the time step for the simulation.

Unlike the trapped particles, which are constrained to sample only one local poloidal magnetic well, the circulating (untrapped) particles are free to sample many oscillations along a magnetic field line. We therefore require that whenever a circulating ion reaches the end of the system at $l = L$, it is reflected with an adiabatic response on the perturbed distribution function. The physical background is that ions must have the same response as electrons when $l \to \infty$. This boundary condition is only valid when the system length is big enough so that the electrostatic potential at the end of the system is much smaller than it's value at or near the origin of the system. In general this will be true when growing modes are present.

The centers of trapped particle orbits are at $\chi_m = 2\pi m_1$, where m_1 is an integer. For a trapped particle the turning points are given by

$$\chi^0 = 2\pi m_1 \pm \cos^{-1}(\frac{\mu B_0}{E} - 1)/\varepsilon. \qquad (15)$$

To find an even solution we need only run one half length of the system, that is, solve for ϕ only for positive values of χ because of the even symmetry of ϕ. In this case,

whenever a particle moves away from the origin of the system, the particle will be replaced by a virtual particle on the other half of the system because of the even symmetry of motion of the particles.

Eqs. (11)-(14) can be solved straightforwardly with the standard numerical particle pushing methods. Our code uses an Euler's first order scheme for Eq. (11) and (13), subtracted dipole weighting for the charge for Eq. (12), and accumulation SM(k) smoothing of the charge density.[30] The time steps were chosen to satisfy the condition $v_{th}\Delta t < \Delta L$, where ΔL is the grid spacing.

In principle, the collision model Eq. (5) has several important general properties: particle conservation, momentum conservation and energy conservation. In order to keep momentum and energy conservation, besides taking into account the changes of the particle orbit given in Eq. (14), one would have to include the last two terms of Eq. (5) into the source such as the last two terms on the right hand side of Eq. (11). One way to do that is to calculate the velocity integrals at each spatial grid point from the continuous particle positions and then calculate the values of the last two terms in Eq. (5) at the particles from the velocity integrals on the grid points by using some form of interpolation. This is demanding statistically. In the problem considered, we found that momentum and energy are adequately conserved over the time scales compared with ion temperature gradient driven instabilities without these terms. Thus, motivated by the analytic results that pitch angle scattering is the dominant effect, we will neglect the last two integral terms in Eqs. (5) and (11) in the simulation.

For the purpose of the linear analysis, we are interested in the dependence of frequency and of structure of the modes on the various physical parameters. The $1\frac{2}{2}d$ code was used to compute the total energy of the systems $\int dl\phi^2(l,t)$ in arbitrary units versus time t in units of ω_{*T}. A typical plot is given in Fig. 1, from which we can measure the growth and the real frequency of the modes. The snapshots of the corresponding poloidal harmonics were plotted at several different times to monitor the mode structure.

The algorithm outlined above, based on δf, has given us a very good benchmark of its numerical efficiency. The code is normally performed on VAX station 3200 with an hour of computer time. Some runs are done on San Diego Supercomputer Cray Y-MP with several

minutes CPU time. This puts a rather bright prospects on the applicability of our approach to cases of practical interest. It is worth pointing out that recently a number of papers have appeared in which the stability properties of ∇T_i mode are studied by either solving the correct integral eigenvalue problem or using a standard particle algorithm in toroidal geometry. The most directly relevant previous calculation is that in Ref. 7 and 31, where a linear integral formulation has been applied to the toroidal study of fully electromagnetic kinetic eigenmodes. The present work differs in several respects. First, with regard to collisional dissipation, the validity and accuracy of the energy and pitch-angle dependent Krook operator used in Refs. 7 and 31 is questionable for intermediate collision frequencies, $\nu/\epsilon \approx |\omega|$. Second, the mode $\phi(x)$ is expanded in Hermite polynomials. As noted by the authers of Refs. 7 and 31, the number of basis functions, L, must be chosen sufficiently large so that the eigenvalue ω is independent of L to some acceptable accuracy. Thus it is quite time-demanding. A first fairly comprehensive two dimensional gyro-kinetic particle simulation of the ∇T_i-mode has been given by Lee for a sheared slab geometry.[32] Along this line an electrostatic, three dimensional standard particle simulation model which follows the electron guiding center motion and gyrophase-averaged ion guiding centers in cylindrical geometry was developed recently to study the linear growth and saturation of trapped electron instabilities. Alternatively, turbulence transport simulations, based on either the kinetic δf particle algorithm[34] or the kinetic δf finite difference grid method[35] in a sheared slab geometry with an adiabatic electron response have been undertaken. By contrast, the main purpose of our linear code is to produce quick, accurate estimate of various thresholds of ∇T_i mode.

IV. Simulation of Slab η_i Modes

The slab η_i mode (which was developed theoretically in the 1960's) is basically a sound wave destabilized when the ion temperature gradient is steeper than the density gradient. Since the first clear evidence (from measurements on DIII-D) that ion heat transport is anomalous[36] and the first indication that the η_i mode was linked to the significant thermal transport in tokamaks,[37] experiments on all subsequent tokamaks have confirmed these observations. With regard to the formal theoretical and experimental basis in support of the relevance of the η_i-modes, linear properties of the mode and the various nonlinear models for χ_i associated with η_i modes have been extensively discussed.[43,44]

In this section, a $1\frac{2}{2}$ gyro-kinetic particle code in a sheared slab geometry, based on the techniques described in section III., has been developed. Formally we can simply let $R_0 \rightarrow \infty$ in our general toroidal code. The simulations of slab η_i modes have been carried out in order to compare with the linear growth, mode structure and threshold condition predictions of theory for the normal density profile. We thus can test the code.

The simulation parameters used were:

$N = 4096$ (the total number of simulation particles), $L = 5000 - 30000\rho_s$ (one half length of system), $ng = L/\Delta L$=128 (number of grids). $\omega_{*i}\Delta t$=0.05, $L_n = 40\rho_s$, $L_{Ti} = 10 - 40\rho_s$, $\eta_i = L_n/L_{Ti} = 4 - 1$, $L_S/L_n = 5, 20$, $k_y\rho_s = 0.2$, $\tau = T_e/T_i = 1$, $R_0 \rightarrow \infty$. The simulations were run from $\omega_{*i}t = 0 - 100$.

The particle positions were initialized with a bit-reversed quiet start (uniform in phase space).

Let us first consider the case with L_S/L_n=5 and 20 in order to verify the linear growth rate and mode structure predicted by theory. Based on adiabatic electrons and small Larmor radius expansion, the linear properties of the modes can be obtained from the solutions of the kinetic eigenmode equation,

$$\rho_s^2 \frac{d^2\phi_k}{dx^2} + [-b_s + \tau \frac{\tau + 1 + (\tau + \frac{1}{\Omega} - \frac{\eta_i}{2\Omega})\xi_i Z(\xi_i) + \eta_i \xi_i^2 \frac{1+\xi_i Z(\xi_i)}{\Omega}}{(\tau + \frac{1}{\Omega} + \frac{\eta_i}{2\Omega})\xi_i Z(\xi_i) + \eta_i \xi_i^2 \frac{1+\xi_i Z(\xi_i)}{\Omega}}]\phi_k = 0. \qquad (16)$$

Here $\Omega = \omega/\omega_{*e}, \xi_i = \omega/(2^{1/2}k_\parallel v_{ti}), b_s = k_\chi^2\rho_s^2$ and $Z(\xi_i)$ is the usual plasma dispersion function for ions with argument ξ_i. Equation (16), which is valid for $(k_x^2 + k_y^2)\rho_i^2 \ll 1$, has

been solved numerically by using a WKB shooting method.

For the case $L_s/L_n = 5$, the resulting linear mode frequencies from the shooting code are $\Omega_{l=0} = (-0.31, 0.17)$ and $\Omega_{l=1} = (-0.93, 0.13)$, and the higher radial harmonics of the eigenmodes are found to be stable. The corresponding frequency from the simulation (which treats only even modes) for the most dominant mode is $\Omega_{l=0} = (-0.22, 0.151)$. The agreement with theory is found to be very good.

In the weaker shear case, $L_s/L_n = 20$, the linear mode frequencies are $\Omega_{l=0} = (-0.05, 0.11)$, $\Omega_{l=1} = (-0.25, 0.22)$ and $\Omega_{l=2} = (-0.43, 0.23)$. The highest radial harmonic of the eigenmodes, namely $l = 2$, is the most unstable. From the simulation the $l = 2$ radial eigenmode is dominant, the frequency $\Omega_{l=2} = (-0.313, 0.19)$ being in good agreement with the shooting method result.

It is well known that for $0 < L_n/L_s \ll 1$, there exists a threshold value of η_i for the normal density profile. Results from a number of numerical studies have indicated that $1 < \eta_i < 2$. In the case where $L_s/L_n = 5$, the shooting method gives the threshold $\eta_{ic} \approx 1.75$, while the simulation shows that $\eta_{ic} \approx 1.25$, which is shown in Fig. 2. The difference between these two values may be understood as follows: as we approach the threshold, the mode width becomes broadened in ballooning space, and Eq. (3. 16), which employed an expansion for small Larmor radius $k_\perp^2 \rho_i^2 \ll 1$, becomes invalid. This can be seen in the resulting linear mode structure shown in Fig. 3, which shows typical poloidal harmonics for $\eta_i = 4$ and $\eta_i = \eta_{ic}$.

The comparisons given here confirm the fact that our gyro-kinetic particle code works well on the slab η_i mode. This lends credence to the comprehensive toroidal gyro-kinetic particle code predictions for the ion temperature gradient mode which will be studied in next section.

V. Simulation of Toroidal ∇T_i-Modes.

In this section we present results obtained when the toroidal geometry for the ∇T_i-mode is taken into account. In short, the problem is that of solving the ion gyro-kinetic equation (11) with the realistic tokamak parameter: L_{Ti}/R_0 and r/R_0. These will introduce the $v_\parallel$ modulation along the orbit due to the equilibrium magnetic field, and therefore add trapped ion dynamics and magnetic curvature drifts including finite banana width. These new ion responses play a crucial role in the stability analysis of the ∇T_i-mode in toroidal plasma which will be studied below.

The plasmas considered here correspond roughly to a typical H-mode discharge in the DIII-D Tokamak with $B_T = 1.7T$, $R_0 = 1.69M$, and $a = 0.63M$. For the region where the anomalous transport associated with microinstabilities is expected to dominate, we focus our interest at the $q(r_0) = 2$ rational surface. From typical equilibrium profile measurements, the local parameters are $r_0 = 0.5M$, $n_e(r_0) = 5.7 \times 10^{19} M^{-3}$, $T_i(r_0) = 500eV$, $\epsilon_0 = r_0/R_0 = 0.3$, and $\nu_i^* \equiv$ effective ion collision frequency/average trapped ion bounce frequncy $= \nu_{ii,eff}/\omega_{bi} = 1.02$.

The simulation parameters used were as follows:

$N = 4096 - 8192$ (the total number of simulation particles), $L = 3\pi q R_0 - 34\pi q R_0$ (one half length of system), $ng = L/\Delta L = 64$ (number of grids), $\omega_{*T}\Delta t = 0.05$, and the simulations were run from $\omega_{*i}t = 0 - 120$. Particle positions were initialized with a random number generator and initial velocity distributions were Maxwellian.

A. Transition From Slab To Toroidal ∇T_i-Mode

As originally formulated in slab geometry, the slab-like ∇T_i-mode evolves when unstable ion acoustic waves couple to radial ion temperature gradients, yielding negative compressibility instabilities. The growth rate is approximately given by $\gamma \approx k_\parallel c_s[(1+\eta_i)/\tau]^{1/2}$ where $k_\parallel \approx k_\chi \Delta x/L_s$. As the aspect ratio becomes very small, the introduction of toroidal curvature and trapped ions in the low plasma collisionality regime change the nature of the mode. In toroidal geometry, the mode has more of a ballooning structure and is driven by both unfavorable magnetic curvature and acoustic waves. The first thing we study is to continuously change the major radius R in units of the DIII-D major radius R_0 from slab ($R \to \infty$) toward toroidal geometry (R=0.4R_0), keeping all other parameters L_{Ti}, L_s, and r_0 fixed, and thus illustrate the toroidal behavior of the ion-temperature-gradient driven drift instabilities. During the transition ($R = \infty \to 0.4R_0$), the corresponding characteristics of toroidal geometry are represented by the ratios $\omega_d/\omega_{*T} = L_{Ti}/R = 0.1R_0/R$ and $\epsilon = r_0/R = 0.3R_0/R$, where r_0 is the radial position of the $q(r_0) = 2$ rational surface.

The results in Fig. 4 show that, for the parameters considered, the basic characteristics of the modes found in the sheared slab calculation persist in the toroidal geometry. However it is important to emphasize that the toroidal geometry calculation does yield new information about the instabilities. Although the pressure of sound waves now has a stabilizing influence, as it propagates ballooning information from the region of bad curvature to the region of favorable curvature, the slab-like ∇T_i branch becomes weakly unstable. The local unfavorable magnetic curvature drift contributes strongly to the destabilization of the mode. The instability becomes an interchange-type mode, which is the cause of the increase in the growth rate shown in the Fig. 4. The mode structure has been changed from "flute-like" to a moderate ballooning structure in the outer part of the torus, which is shown in Fig. 5. The instability properties described here are similar to those which can be obtained approximately in the fluid-ion limit of the eigenmode analysis. For the same parameters as used in Fig. 4, the two unstable branches have been found with the toroidicity-induced ∇T_i branch being dominant.[13] As the aspect ratio becomes smaller, so that more ions are trapped in local equilibrium magnetic wells, the radial mode width gets broader and the modes experience strong dissipation (ion Landau damping). Thus, the fat

torus provides a stabilizing effect on the ∇T_i-mode.

B. General Dispersion Relation Of ∇T_i-Mode

In the toroidal geometry, the relevance of microinstabilities to tokamaks is associated with the well-known trapped ion modes and the toroidal branch of ion temperature gradient driven ion modes, which are separated by ω_{bi} and ω_{ti}, these being the typical ion bounce and transit frequencies. In the frequency range $\omega \ll (nq-m)\omega_{bi}$, $(nq-m)\omega_{ti}$, the trapped ion modes are low frequency, long wavelength instabilities, which are radially localized halfway between rational surfaces. The modes have interchange character with the growth rate γ given by $\gamma \approx \epsilon^{1/4}\sqrt{\omega_{*T}\omega_d}$. Since the growth is proportional to the population of trapped ions, we can anticipate that near the edge of the plasma ($2 \geq q(r_0) \geq 1$), the trapped ion modes should make great contributions. In contrast, in the frequency range $\omega \gg (nq-m)\omega_{ti}$, $(nq-m)\omega_{bi}$, the toroidal branch of ∇T_i-modes consists of high frequency and short wavelength fluid-like modes, which are localized radially around rational surfaces. As stated in the subsection A, this mode also has interchange character with growth rate given by $\gamma \sim \sqrt{\omega_{*T}\omega_d}$. The interesting point raised recently by Chen *et al.*[13] is that even in long-wavelength limit, the toroidal branch ∇T_i driven fluid-like mode still exists, corresponding to a broader eigenfunction in ballooning space due to the perturbative character of the curvature term. These qualitative features of the ∇T_i-driven instabilities have been obtained in our particle simulations. The results in Fig. 6 present a unified picture of the well-known collisionless fluid-like toroidal induced ∇T_i modes over all wavelengths. For $\tau = 1$, $q(r_0) = 2$, $\hat{s} = 1$, $L_{Ti}/R_0 = 0.1$, $\nu_i^* = 0.0$, the growth of the modes is peaked at $k_\chi \rho_i \approx 0.2$ and becomes stabilized around $k_\chi \rho_i \approx 1.0$ by ion Landau damping. However, the modes remain unstable in the very long wavelength limit ($k_\chi \rho_i \approx 0.01$). Any further examination of long wavelength modes would violate the ballooning mode representation assumption ($nq \gg 1$) made in deriving Eq. (1). Thus, to properly investigate the $k_\chi \rho_i \leq 0.01$ regime, we would need to carry out a two dimensional analysis. Fortunately, when ion-ion collisions are included, the long wavelength modes become stabilized, as is shown in Fig. 7 for the same parameters as in Fig. 6 except $\nu_i^* = 1.02$. Unlike the high frequency limit results, which exhibit an insensitivity to

collisional effects for small collisionality rates, ion-ion collisional dissipation can stabilize the mode at the long wavelength limit around $k_\chi \rho_i \leq 0.015$, since $\nu_{ii} \gg \omega$ at this regime. This result is in qualitative agreement with our previous theoretical studies of the stability of collisional trapped ion modes in flat density discharges. The actual marginal stability curve can be determined analytically in the collisional trapped ion driven ∇T_i-mode limit for $\eta_i \gg 1$ and ω, $\nu_{ii,eff} \gg \omega_d$, yielding:[27]

$$\eta_{ic} = 0.65 \frac{\nu_{ii,eff}}{\omega_{*i}} \frac{1+\tau^{-1}}{\sqrt{2\epsilon}}.$$

The analytic value of the stability threshold for parameters considered here is $k_\chi \rho_i \leq 0.06$. Note that the boundary for $k_\chi \rho_i$ given by the simulation is roughly in a factor of 4 decrease over one given by the theory. A possible explanation of this difference is due to strong ballooning eigenmode approximation made in the theory. The eigenmode structures corresponding to short and long wavelength limits are shown on Fig. 8 for $k_\chi \rho_i = 0.6$ and $k_\chi \rho_i = 0.025$ respectively.

The stability of ∇T_i-driven modes is also determined by several other dimensionless parameters: τ and $\hat{s}$. Fig. 9 illustrates the complex frequency ω values for various values of $\tau = T_e/T_i$ for fixed $k_\chi \rho_i = 0.1$, $L_{Ti}/R_0 = 0.1$, $\nu_i^* = 0$. The magnetic shear dependence $\hat{s}$ of the modes is plotted in Fig. 10 for fixed $L_{Ti}/R_0 = 0.1$, $k_\chi \rho_i = 0.1$ and $\nu_i^* = 0.0$.

C. Relation Between Long Wavelength Limit ∇T_i-Mode and Trapped Ion Modes

It is reasonable to ask whether or not the mode representation described in Sec. II. is able to account for the ∇T_i driven trapped ion modes since they are radially localized halfway between the rational surfaces. The basic assumption of ballooning mode representation comes to mind. Phenomena that can be described in the ballooning representation are constant along and rapidly varying perpendicular to the magnetic fields, and have radial variations on the order of the distance between adjacent mode rational surfaces. This puts a constraint on $k_\chi \rho_i$ such that $(k_\chi \rho_i)$ min $r_0/\rho_i = nq \gg 1$. For the DIII-D tokamak parameters considered above, $k_\chi \rho_i = 0.01$ gives nq = 4-5. In the ballooning representation the extended poloidal angle χ and the rapidly varying radial variable $\overline{S} = (nq - m)$ are conjugate through the Fourier transform:

$$\phi(\overline{S}) = \frac{1}{2\pi} \int_{-\infty}^{\infty} d\chi \phi(\chi) e^{i\overline{S}(\chi - \chi_0)}. \qquad (17)$$

Thus radial locations of the modes should be able to be determined from the parameter χ_0 in the ballooning hierarchy. For example, if the mode has a Gaussian form in χ,

$$\phi(\chi) = c e^{-\alpha \chi^2},$$

we obtain $\phi(\overline{S})$ from Eq. (17)

$$\phi(\overline{S}) = \frac{c}{2\sqrt{\pi\alpha}} e^{-\frac{1}{\alpha}[(\overline{S}/2) - i\alpha\chi_0]^2 - \alpha\chi_0^2}.$$

Hence, $\phi(\overline{S})$ is a Gaussian centered at the radial position $\overline{S}_0 = 4\alpha_m \chi_0$, where α_m is the imaginary part of mode width α. On the mode rational surfaces we have $\chi_0 = 0$, whereas on the mode half-rational surfaces, where $\overline{S}_0 = 1/2$, we have $\chi_0 = 1/8\alpha_m$. Lacking a definitive calculation of the mode width α_m, χ_0 has been treated as an adjustable parameter in the simulations. The largest growth rate as a function of χ_0 is the relevant one. In our case where electrons are adiabatic we always find $\chi_0 = 0$ to be the worst value, as is expected for the type of up-down symmetric equilibrium considered here.

The results of interest are displayed in Fig. 11 and Fig. 12 for $k_\chi \rho_i = 0.1$ and $k_\chi \rho_i = 0.025$. Figure 11 shows that the χ_0 has a stronger influence on the short wavelength ∇T_i-mode than it does in the long wavelength limit. Indeed, as χ_0 is artificially increased from 0

to π the radial location of the mode moves rapidly away from the mode rational surface, and consequently experiences more ion Landau damping. The long wavelength limit behavior, however, is observed to be fairly insensitive to χ_0, as is shown in Fig. 12. This characteristic behavior of ω as a function of χ_0 can be best understood by examing the poloidal structure of the instabilities in Fig. 8. As stated, the width of this long wavelength mode structure is very broad ($\Delta\chi > 2\pi$). Hence, in this case χ_0 only changes the poloidal location of the potential well, with little influence on the structure. It is important to emphasize that the long wavelength ∇T_i-driven fluid-like mode and ∇T_i driven trapped ion mode are two different kinds of modes with different radial location. However, both modes exhibit a weak ballooning poloidal structure with comparable growth and frequencies and are susceptible to ion-ion collisional stabilization.

D. Threshold Condition For L_{Ti}/R_0

In order to determine the qualitative properties of the ∇T_i-mode marginal instability, a simple fluid ion mode ($\omega \gg k_\parallel v_{Ti}$) in the flat density gradient limit, containing the essential physics, has been studied recently by several authors.[8-12] The results of these local analyses show that the potentially interchange type destabilizing ($\omega_* \omega_d > 0$) contribution due to adverse magnetic curvature can be completely stabilized by a complex interplay of several physical effects: magnetic drift frequency resonance (perpendicular compression in MHD approximation), finite ion Larmor radius effects, and sound wave coupling. The values of the stability threshold have been calculated based on the various kinetic models, and are suspect in accuracy. In this section, we present a comprehensive stability analysis, which more accurately maps out stability boundaries over several dimensionless parameters: L_{Ti}/R_0, $k_\chi \rho_i$ and τ. The results for ω and L_{Ti}/R_0 are shown in Fig. 13 through 15 where we vary the parameters L_{Ti}/R_0, $k_\chi \rho_i$ and τ. In all figures we have fixed $\hat{s} = 1$ and $q(r_0) = 2$. In Fig. 13, the imaginary and real parts of the frequency are plotted versus L_{Ti}/R_0 with $k_\chi \rho_i = 0.05$, 0.2 and 0.6 for collisionless cases. In this case, collisionality make little difference for the value of the threshold L_{Ti}/R_0, as noted in the subsection B. Since the structures of eigenfunctions are almost the same when L_{Ti}/R_0 is varied, it can now be argued that magnetic drift frequency resonance (or perpendicular compression) make a

great contribution to the stabilization of the ∇T_i-mode for fixed $\hat{s}$ and τ. In Fig. 14, the unstable region in L_{Ti}/R_0—$k_\chi \rho_i$ is shown for $\tau = 1$. The maxima in the curves occurs at $L_{Ti}/R_0 \approx 0.255$ at the most unstable mode $k_\chi \rho_i = 0.2$. The marginal stability boundaries L_{Ti}/R_0 with $\tau = T_e/T_i$ is plotted in Fig. 15 for $k_\chi \rho_i = 0.1$ and $k_\chi \rho_i = 0.2$. Note that for hot-ion mode ($\tau < 1$), the ∇T_i-mode has a lower value for the threshold L_{Ti}/R_0, which is in agreement with the experimental observation in DIII-D of hot ion H-mode discharges.[14] These threshold ratios are previously calculated based on the different model. The most complete calculation is that in Ref. 9, where both the numerical and analytical analysis of full kinetic limit retains magnetic drift resonance effects and the ion transit resonance but assumes to have no trapped ion dynamics, and obtains analytically an actual marginal stability curve for CER approximation of magnetic drift frequency:

$$\eta_{ic} = \frac{4}{3}(1 + \tau^{-1})\epsilon_n.$$

For large value of $\epsilon_n = L_n/R_0$, the above formula yields $L_{Ti}/R_0 = 0.37$ for $\tau = 1.0$ and $L_{Ti}/R_0 = 0.25$ for $\tau = 0.5$. We note, however, that our numerical results predict much lower critical values of L_T/R_0, in better agreement with experiment.

E. Transition From η_i-Mode To Flat Density ∇T_i-Mode

Previous sections have investigated the physics in so-called H-mode discharges where the ion density can be assumed to be nearly flat (Ln$\rightarrow \infty$). One of the interesting phenomena particularly relevant to H-mode plasmas is that while electron density profiles on DIII-D, for example, have been observed to be relatively flat, the corresponding Z_{eff} profiles appear to be centrally peaked.[4] H-mode discharges with outwardly peaked electron density profiles have been measured in both the DIII-D and the JET tokamaks.[4,6] Motivated by these experimental observation, previous theoretical studies have proposed negative η_i-type drift instabilities.[12] The investigation of normal ($\eta_i > 0$), flat ($\eta_i \rightarrow \infty$), and inverted ($\eta_i < 0$) ion density profile scenarios thus complete the ion temperature gradient driven drift instabilities. Based on these considerations, the comparison between negative and positive η_i cases is made in Fig. 16 when η_i is varied for fixed $L_{Ti}/R_0 = 0.1$, $k_\chi \rho_i = 0.1$, $\nu_i^* = 0.0$ and $\tau = 1$. As expected, when $|\eta_i| \gg 1$ is satisfied the complex mode

frequencies are almost symmetric with respect to the sign of η_i. However, even though the growth rates are almost symmetric with respect to the sign of η_i, the properties of the negative η_i-mode are quite different from those of ion temperature gradient modes either with $\eta_i > 0$ or with flat ion density gradients ($\eta_i \to \infty$), since $\gamma \ll |\omega_r|$ holds for negative η_i-modes over a wide range of negative η_i values. This differs considerably from the positive η_i or flat density gradient cases where $\gamma \ll |\omega_r|$ is satisfied only near the threshold $\eta_{ic}^{(+)}$ or L_{Ti}/R_0. Similar features for the inverted density profile cases have also been observed in the sheared slab geometry. The implications for the new features of the negative η_i modes is that a weak turbulence analysis of the resultant confinement characteristics is reasonable.

F. Effect of Finite $\epsilon\beta_p$ on the ITG Mode

In this section, we investigate the effect of a large pressure gradient (∇P) on the ITG mode. The dominant effect of high poloidal beta is to modify the local shear and the gradient of the magnetic field strength. Motivated by the analytic results that at high poloida beta, the electromagnetic coupling is small both in the slab[40] and trapped ion driven ITG mode analysis,[27] we will study the electrostatic dispersion relation in the high beta equilibrium. The finite $\epsilon\beta_p$ and the real geometry effects enter in evaluating J, $k_\perp$ and ω_d, where J is the Jacobian which gives relation between the magnetic field length l and the poloidal angle χ, $dl = JBd\chi$. At zero beta and near the plasma axis the equilibrium is well approximated by $J = (qR_0)/B_0$ and Eq. (4a). At high poloida beta we use the $s - \alpha$ approximation to the equilibrium to gain insights into equilibrium effects.[19] In this case, Eq. (4a) will be changed to the following form:

$$\vec{k}_\perp = n\nabla S = -k_\theta[\vec{e}_\theta + h(\theta)\vec{e}_r]$$

$$\omega_{dj} = \frac{k_\chi}{2R_0\Omega}\{(v^2 + v_\parallel^2)[\cos\chi + h(\chi)\sin\chi] - v_\perp^2\frac{1}{4}\frac{\alpha}{q^2}\}$$

$$h(\chi) = \hat{s}\chi - \alpha\sin\chi$$

$$\frac{\partial}{\partial l} = (\vec{b}\cdot\nabla\chi)\frac{\partial}{\partial\chi} = \frac{1}{R_0 q}\frac{\partial}{\partial\chi}$$

Where $\alpha = -q^2R_0 d\beta/dr$ is a measure of the local Shafranov shift, with $\beta \equiv 8\pi\sum n_j T_j/B_0^2$. The Jacobian is the same as in the zero beta case.

The above finite poloidal beta correction have been put into the code described in Sec. III. The results are shown in Fig. 17 with $k_\chi \rho_i = 0.2$, $\hat{s} = \tau = 1$, $L_{Ti}/R_0 = 0.1$, $\nu_i^* = 0.0$ and $\eta_i = \infty$. A reduction of growth rate of ITG mode is evident as α increases. This picture is in qualitative agreement with our previous analytic calculation where the trapped ion driven ∇T_i-mode can be stabilized by increased plasma diamagnetism. Combining strong ballooning structure of eigenfunction and high poloidal beta effects, we obtain analytically a marginal stability curve for the collisionless trapped ion driven ∇T_i-mode:[27]

$$\alpha_{cr} = \frac{1.71 + \hat{s}}{1 + \frac{7}{6q^2}}$$

For the same parameters as used in Fig. 17, the analytical stability threshold of the trapped ion driven ∇T_i-mode is $\alpha_{cr} = 2.1$. Such favorable finite-β effects may provide an explanation of the good edge confinement in H-mode associated with the sharp pressure gradients.

VI. Discussion And Conclusions

In this paper a general procedure has been presented for the application of gyro-kinetic particle simulation techniques, by the δf algorithm developed in the ballooning mode formalism, to low-frequency microinstabilities in a toroidal geometry. A complete treatment of the ion temperature gradient driven instabilities including trapped-particle and banana effects has been presented. In addition, a new scheme of a linearized ion-ion collision operator has been developed within the framework of the gyro-kinetic formalism. Numerical results from slab η_i mode are found to be in reasonable agreement with corresponding results for eigenvalues and eigenfunctions from the extensively used WKB shooting method or previous particle simulations in the limit $\eta_i \gg \eta_{ic}$. Finally, the investigation of the ∇T_i modes in toroidal geometry has provided us with considerable insight into the unified account of electrostatic ion-temperature-gradient-driven drift wave instabilities over all parameter regimes.

The main result of the present investigation is the evaluation of the L_{Ti}/R_0 threshold for the full kinetic model. The threshold has a significant dependence on the parameters $\tau = T_e/T_i$ and magnetic shear parameter $\hat{s}$. For $\tau = \hat{s} = 1$, we found that $L_{Ti}/R_0 \approx 0.255$. However, the threshold is lower at low values of τ, i.e., in the hot-ion H-mode

discharges. For $\tau = 0.5$ and $\hat{s} = 1$, we obtain critical $L_{Ti}/R_0 = 0.16$. These trends are qualitatively consistant with the experimental observation on DIII-D hot-ion H-mode discharges.[14] However the critical value of L_{Ti}/R_0 is still higher than the observed value which is about 0.1. Given the strong influence of the magnetic shear parameter $\hat{s}$ on the ∇T_i-mode, we conjecture that taking into account the realistic internal flux surface shapes and poloidally varying shear with elongation and triangularity will reduce our critical L_{Ti}/R_0 towards the observed value. The analysis given here is in support of the argument that the anomalous ion thermal transport in DIII-D H-mode discharges should be controlled by ITGDT marginal stability.

In addition to a more realistic treatment of geometry, the most important remaining development needed for the present analysis is electron dynamics. As discussed in the introduction, nonadiabatic electron dynamics make a negligible contribution to ∇T_i-driven instabilities in the flat density limit on H-mode discharges. However, for the peaked density profiles in L-mode discharges, both η_i-drift instabilities and trapped-electron modes could play an important role. In particular, as is indicated by Romanelli *et al.*[9] and Rewoldt *et al.*[41], the effect of trapped electrons on the η_i-mode stability is to remove the threshold $\eta_i = \eta_{ic}$. Thus the usual η_i mode was seen to connect to the usual collisionless trapped electron mode as η_i decreased, while the propagation direction of the mode changed from the ion diamagnetic direction to the electron diamagnetic direction. Therefore the above development would allow us to apply our analysis to this "soft" η_i threshold regime of L-mode operation and provide meaningful comparison with the experimental observations. It is anticipated that other improvements, such as a systematic treatment of the influence of electromagnetic (finite-β) effects and of more complicated toroidal equilibria on ∇T_i-driven instabilities will likely necessitate the further application of this approach.

VII. Appendix.

The Fokker-Planck collision term for an inverse-square force was derived by Rosenbluth *et al.* (1957) in the form[38]

$$C(f_\alpha) = -\frac{\partial}{\partial \vec{v}} \cdot (\frac{< \Delta \vec{v} >_{\alpha\beta}}{\Delta t} f_\alpha) + \frac{1}{2} \frac{\partial^2}{\partial \vec{v} \partial \vec{v}} : (\frac{< \Delta \vec{v} \Delta \vec{v} >_{\alpha\beta}}{\Delta t} f_\alpha), \tag{A.1}$$

where

$$\frac{< \Delta \vec{v} >_{\alpha\beta}}{\Delta t} = \Gamma_{\alpha\beta} \frac{\partial}{\partial \vec{v}} H_\beta(\vec{v}), \tag{A.2}$$

$$\frac{< \Delta \vec{v} \Delta \vec{v} >_{\alpha\beta}}{\Delta t} = \Gamma_{\alpha\beta} \frac{\partial^2}{\partial \vec{v} \partial \vec{v}} G_\beta(\vec{v}), \tag{A.3}$$

in which

$$\Gamma_{\alpha\beta} = \frac{4\pi {q_\alpha}^2 {q_\beta}^2}{m_\alpha^2} \ln \Lambda_{\alpha\beta}, \tag{A.4}$$

and

$$G_\beta(\vec{v}) = \int d^3v' f_\beta(v') |\vec{v} - \vec{v}'|, \tag{A.5}$$

$$H_\beta(\vec{v}) = \frac{m_\alpha}{m_{\alpha\beta}} \int d^3v' \frac{f_\beta(\vec{v}')}{|\vec{v} - \vec{v}'|} = (1 + \frac{m_\alpha}{m_\beta}) \int d^3v' \frac{f_\beta(\vec{v}')}{|\vec{v} - \vec{v}'|}. \tag{A.6}$$

The G_beta and H_β functions are the so-called Rosenbluth potentials. The dynamical friction $< \Delta \vec{v} >_{\alpha\beta} / \Delta t$ and velocity diffusion coefficients $< \Delta \vec{v} \Delta \vec{v} >_{\alpha\beta} / \Delta t$ are related as follows

$$\frac{< \Delta \vec{v} >_{\alpha\beta}}{\Delta t} = (1 + \frac{m_\alpha}{m_\beta}) \frac{\partial}{\partial \vec{v}} \cdot \frac{< \Delta \vec{v} \Delta \vec{v} >_{\alpha\beta}}{\Delta t}. \tag{A.7}$$

The linearized Fokker-Planck equation is

$$\begin{aligned} C(f_\alpha^1) = & -\frac{\partial}{\partial \vec{v}} \cdot (\frac{< \Delta \vec{v} >^0_{\alpha\beta}}{\Delta t} f_\alpha^1) + \frac{1}{2} \frac{\partial^2}{\partial \vec{v} \partial \vec{v}} : (\frac{< \Delta \vec{v} \Delta \vec{v} >^0_{\alpha\beta}}{\Delta t} f_\alpha^1) \\ & \underline{-\frac{\partial}{\partial \vec{v}} \cdot (\frac{< \Delta \vec{v} >^1_{\alpha\beta}}{\Delta t} f_\alpha^0) + \frac{1}{2} \frac{\partial^2}{\partial \vec{v} \partial \vec{v}} : (\frac{< \Delta \vec{v} \Delta \vec{v} >^1_{\alpha\beta}}{\Delta t} f_\alpha^0).} \\ & pF_m \end{aligned} \tag{A.8}$$

The calculations of $< \Delta \vec{v} >^0_{\alpha\beta}$ and $< \Delta \vec{v} \Delta \vec{v} >^0_{\alpha\beta}$ will be based on the assumption that the test particle is colliding with a plasma whose components have Maxwellian distributions; $< \Delta \vec{v} >^1_{\alpha\beta}$ and $< \Delta \vec{v} \Delta \vec{v} >^1_{\alpha\beta}$ are, in general, evaluated using f^1_β, which are

not sensitive to the detail of f_α^1. Thus, rather than use such a complicated form it is convenient to employ a simpler p determined by the conservation of momentun and energy constraints in that the momentum and energy removed by the first two terms in Eq. (A.8) is replenished in a Maxwellian distribution by the pF_m term.[39]

From the linearized Fokker-Planck equation (A.8), we have

$$C(f_\alpha^1) - pF_m = -\frac{\partial}{\partial \vec{v}} \cdot (\frac{< \Delta \vec{v} >_{\alpha\beta}^0}{\Delta t} f_\alpha^1) + \frac{1}{2} \frac{\partial^2}{\partial \vec{v} \partial \vec{v}} : (\frac{< \Delta \vec{v} \Delta \vec{v} >_{\alpha\beta}^0}{\Delta t} f_\alpha^1). \tag{A.9}$$

Specific test particle collisional effects due to dynamical friction and velocity diffusion can be worked out for a Maxwellian velocity distribution of background particles:

$$f_\beta(\vec{v}) = n_\beta (\frac{m_\beta}{2\pi T_\beta})^{\frac{3}{2}} e^{-m_\beta v^2/2T_\beta} = \frac{n_\beta e^{-v^2/2v_{T\beta}^2}}{(2\pi)^{\frac{3}{2}} v_{T\beta}^3}. \tag{A.10}$$

The Rosenbluth potential $G_\beta(\vec{v})$ for Maxwellian background particles can be written as

$$G_\beta(\vec{v}) = n_\beta v_{T\beta} \frac{\sqrt{2}}{\sqrt{x}} [(x+1)\Psi'(x) + (x + \frac{1}{2})\Psi(x)], \tag{A.11}$$

in which

$$\Psi(x) = \frac{2}{\sqrt{\pi}} \int_0^x dt \sqrt{t} e^{-t}, \tag{A.12}$$

$$x = x^{\alpha/\beta} = \frac{\overline{v}^2}{2} = m_\beta v^2/2T_\beta = v^2/2v_{T\beta}^2, \tag{A.13}$$

where x is the square of the ratio of the test particles speed to the thermal speed of the background particles. $\Psi(x)$ is the Maxwell integral, which has the properties:

$$\Psi' = \frac{d\Psi}{dx} = \frac{2}{\sqrt{\pi}} \sqrt{x} e^{-x}, \Psi + \Psi' = \frac{2}{\sqrt{\pi}}.$$

Thus, for a Maxwellian velocity distribution of background particles the Rosenbluth potential is $G_\beta(\vec{v}) = G_\beta(v)$, i.e., it depends only on the test particle speed v and not its velocity $\vec{v}$. Substituting the Rosenbluth potential in (A.11) into (A.3) and (A.7), we find that the relevant dynamical friction and velocity diffusion coefficients are given by

$$\frac{< \Delta \vec{v} >^{\alpha/\beta}}{\Delta t} = \Gamma_{\alpha\beta} \frac{m_\alpha}{2m_\beta} \frac{\partial}{\partial \vec{v}} \cdot [\vec{I} \frac{1}{v^2} \frac{\partial}{\partial v} (v^2 \frac{\partial G_\beta}{\partial v})]$$

$$= -[(1+\frac{m_\alpha}{m_\beta})\Psi(x^{\alpha/\beta})]\nu_0^{\alpha/\beta}\vec{v}, \tag{A.14}$$

$$\frac{<\Delta\vec{v}\Delta\vec{v}>^{\alpha/\beta}}{\Delta t} = \Gamma_{\alpha\beta}\frac{\partial^2}{\partial\vec{v}\partial\vec{v}}G_\beta(v)$$
$$= \Gamma_{\alpha\beta}\frac{\partial}{\partial v}G_\beta(v)\frac{\vec{I}}{v}$$
$$+ \Gamma_{\alpha\beta}[\frac{\partial^2}{\partial v^2}G_\beta(v) - \frac{1}{v}\frac{\partial}{\partial v}G_\beta(v)]\frac{\vec{v}\vec{v}}{v^2}. \tag{A.15}$$

The reference collision frequency for all these processes is defined by

$$\nu_0^{\alpha/\beta}(v) = \frac{4\pi n_\beta q_\alpha^2 q_\beta^2}{m_\alpha^2 v^3}\ln\Lambda_{\alpha\beta}. \tag{A.16}$$

Therefore Eq. (A.9) can be written as

$$C(f^1) - pF_m = \frac{\partial}{\partial\vec{v}}\cdot(\vec{v}Ff^1) + \frac{\partial^2}{\partial\vec{v}\partial\vec{v}} : [G\vec{I} + H\frac{\vec{v}\vec{v}}{v^2}]f^1, \tag{A.17}$$

where

$$F = +2\Psi(x)\nu_0 = [(1+\frac{m_\alpha}{m\beta})\Psi(x^{\alpha/\beta})]\nu_0^{\alpha/\beta},$$
$$G = \frac{1}{2v}\Gamma_{\alpha\beta}\frac{\partial G_\beta(v)}{\partial v}$$
$$= \frac{1}{2}v^2[\Psi(x)(1-\frac{1}{2x}) + \Psi'(x)]\nu_0,$$
$$H = \frac{1}{2}\Gamma_{\alpha\beta}[\frac{\partial^2}{\partial v^2}G_\beta(v) - \frac{1}{v}\frac{\partial}{\partial v}G_\beta(v)]$$
$$= -\frac{1}{2}v^2[\Psi(x)(1-\frac{3}{2x}) + \Psi'(x)]\nu_0.$$

In Eq. (A.8) conservation of number is automatic and p is determined from conservation of momentum and energy. Taking

$$p = \vec{v}\cdot\vec{p} + \lambda[\frac{v^2}{2{v_T}^2} - \frac{3}{2}], \tag{A.18}$$

p and λ are determined from conservation of momentum and energy respectively:

$$\vec{p} = \frac{1}{n_0{v_T}^2}\int d^3v\vec{v}Ff^1, \tag{A.19}$$
$$\lambda = \frac{2}{3n_0{v_T}^2}\int d^3v[v^2F - 3G - H]f^1.$$

The final modified Fokker-Planck collision operator is in the form:

$$\begin{aligned} C(f^1) =& \frac{\partial}{\partial \vec{v}} \cdot (\vec{v} F f^1) + \frac{\partial^2}{\partial \vec{v} \partial \vec{v}} : [G\vec{I} + H\frac{\vec{v}\vec{v}}{v^2}] f^1 \\ &+ \frac{F_m}{n_0 {v_T}^2} \vec{v} \cdot \int d^3 v \vec{v} (vF) f^1 \\ &+ (\frac{v^2}{2{v_T}^2} - \frac{3}{2}) \frac{2F_m}{3n_0 {v_T}^2} \int d^3 v [v^2 F - 3G - H] f^1. \end{aligned} \tag{A.20}$$

To develop the Monte-Carlo method for the particle simulation, we introduce cylindrical coordinates $(v_\parallel, v_\perp, \varphi)$. We note

$$\begin{aligned} \frac{\partial}{\partial \vec{v}} \cdot \frac{\vec{v}}{v^3} &= 4\pi \delta(\vec{v}), \\ \frac{\partial}{\partial \vec{v}} \cdot \frac{\vec{v}\vec{v}}{v^4} &= \frac{\vec{v}}{v} 4\pi \delta(\vec{v}), \\ \Delta_v^2 =& \frac{1}{v_\perp} \frac{\partial}{\partial v_\perp} v_\perp \frac{\partial}{\partial v_\perp} + \frac{\partial^2}{\partial v_\parallel^2} + \frac{1}{v_\perp^2} \frac{\partial^2}{\partial \varphi^2} \\ =& 4 \frac{\partial^2}{(\partial v_\perp^2)^2} v_\perp^2 - 4 \frac{\partial}{\partial v_\perp^2} + \frac{\partial^2}{\partial v_\parallel^2} + \frac{1}{v_\perp^2} \frac{\partial^2}{\partial \varphi^2}, \\ \frac{\partial}{\partial v} =& \frac{\vec{v}}{v} \cdot \frac{\partial}{\partial \vec{v}} = \frac{2v_\perp^2}{v} \frac{\partial}{\partial v_\perp^2} + \frac{v_\parallel}{v} \frac{\partial}{\partial v_\parallel}. \end{aligned}$$

Eq. (A.20) can be rewritten in the form

$$\begin{aligned} C(f^1) =& \frac{\partial}{\partial v_\perp^2} [\nu_{s\perp}(v_\perp^2, v) v^2] f^1 + \frac{\partial}{\partial v_\parallel} [\nu_{s\parallel}(v) v_\parallel f^1] \\ &+ \frac{1}{2} \frac{\partial^2}{(\partial v_\perp^2)^2} [\nu_\perp(v_\perp^2, v) v^4 f^1] + \frac{1}{2} \frac{\partial^2}{\partial v_\parallel^2} [\nu_\parallel(v_\parallel^2, v) v^2 f^1] \\ &+ \frac{\partial^2}{\partial v_\perp^2 \partial v_\parallel} [\nu_{\parallel\perp}(v_\parallel, v_\perp) v^3 f^1] + \frac{1}{v_\perp^2} \frac{\partial^2}{\partial \varphi^2} (G f^1) + \frac{F_m}{n_0 v_T^2} \vec{v} \int d^3 v \vec{v} F f^1 \\ &+ (\frac{v^2}{2v_T^2} - \frac{3}{2}) \frac{2F_m}{3n_0 v_T^2} \int d^3 v [v^2 F - 3G - H] f^1, \end{aligned} \tag{A.21}$$

where

$$\begin{aligned} \nu_{s\perp}(v_\perp^2, v) =& 2\frac{v_\perp^2}{v^2} F - \frac{4G}{v^2} - 2\frac{v_\perp^2}{v^4} H \\ =& + 4\Psi(x) \frac{v_\perp^2}{v^2} \nu_0 - 2[\Psi(x)(1 - \frac{1}{2x}) + \Psi'(x)] \nu_0 \\ &+ \frac{v_\perp^2}{v^2} \nu_0 [\Psi(x)(1 - \frac{3}{2x}) + \Psi'(x)], \end{aligned} \tag{A.22}$$

$$\nu_{s\parallel}(v) = +2\Psi(x)\nu_0 = F, \tag{A.23}$$

$$\begin{aligned}\nu_{\perp}(v_{\perp}^2, v) =& 2\cdot[4v_{\perp}^2 G + 4\frac{v_{\perp}^4}{v^2}H]\frac{1}{v^4}\\ =& 4\frac{v_{\perp}^2}{v^2}[\Psi(x)(1-\frac{1}{2x})+\Psi'(x)]\nu_0\\ & -4\frac{v_{\perp}^4}{v^4}[\Psi(x)(1-\frac{3}{2x})+\Psi'(x)]\nu_0,\end{aligned} \tag{A.24}$$

$$\begin{aligned}\nu_{\parallel}(v_{\parallel}^2, v) =& \frac{2}{v^2}[G+\frac{v_{\parallel}^2}{v^2}H]\\ =& [\Psi(x)(1-\frac{1}{2x})+\Psi'(x)]\nu_0\\ & -\frac{v_{\parallel}^2}{v^2}[\Psi(x)(1-\frac{3}{2x})+\Psi'(x)]\nu_0,\end{aligned} \tag{A.25}$$

$$\nu_{\parallel\perp}(v_{\parallel}, v_{\perp}) = \frac{1}{v^3}\cdot 4\frac{v_{\perp}^2 v_{\parallel}}{v^2}H = 2\frac{v_{\perp}^2 v_{\parallel}}{v^3}[\Psi(x)(1-\frac{3}{2x})+\Psi'(x)]\nu_0. \tag{A.26}$$

Now Eq. (A.21) is ready for gyro-averaging. We assume

$$f^1 = -\frac{eF_m}{T}\phi + h_i e^{-iL}, L = k_{\perp}\frac{v_{\perp}}{\Omega}cos\varphi. \tag{A.27}$$

The gyro-averaged Fokker-Planck collision operator is of the form

$$\begin{aligned}< e^{iL}C(e^{-iL}h_i) >=& \frac{\partial}{\partial v_{\perp}^2}\left(\nu_{s\perp}(v_{\perp}^2, v)v^2 h_i\right) + \frac{\partial}{\partial v_{\parallel}}\left(\nu_{s\parallel}(v)v_{\parallel}h_i\right)\\ & + \frac{1}{2}\frac{\partial^2}{(\partial v_{\perp}^2)^2}\left(\nu_{\perp}(v_{\perp}^2, v)v^4 h_i\right) + \frac{1}{2}\frac{\partial^2}{\partial v_{\parallel}^2}\left(\nu_{\parallel}(v_{\parallel}^2, v)v^2 h_i\right)\\ & + \frac{\partial^2}{\partial v_{\perp}^2 \partial v_{\parallel}}\left(\nu_{\parallel\perp}(v_{\parallel}, v_{\perp})v^3 h_i\right) - \frac{k_{\perp}^2}{2\Omega^2}(2G+\frac{v_{\perp}^2}{v^2}H)h_i\\ & + \frac{F_m}{n_0 v_T^2}\left(v_{\parallel}J_0\int d^3v v_{\parallel}J_0 F h_i + v_{\perp}J_1\int d^3v v_{\perp}J_1 F h_i\right)\\ & + (\frac{v^2}{2v_T^2}-\frac{3}{2})\frac{2F_M}{3n_0 v_T^2}J_0\int d^3v(v^2F - 3G - H)J_0 h_i.\end{aligned} \tag{A.28}$$

From Eq. (A.28) we find that the mean parallel and perpendicular components of the test particle velocity after a short time Δt are

$$\overline{v}_{\parallel}' = v_{\parallel}[1-\nu_{s\parallel}(v)\Delta t], \tag{A.29}$$

$$\overline{v'^2}_{\perp} = v^2{}_{\perp} - v^2\nu_{s\perp}(v_{\perp}^2, v)\Delta t. \tag{A.30}$$

This result is valid for $\nu_{s\|}\Delta t \ll 1$, $\nu_{s\perp}\Delta t \ll 1$ and indicates the monotonic decrease of parallel test particle momentum due to Coulumb collisions.

The perpendicular and parallel velocity diffusion processes indicated by $\nu_\perp(v_\perp^2, v)$, $\nu_\|(v_\|^2, v)$, and $\nu_{\|\perp}(v_\|, v_\perp)$ have to be treated differently. Because they are diffusive, they lead to a probability distribution $p(\vec{v} - \bar{\vec{v}})$ of the velocity about the mean velocity given in Eqs. (A.29) and (A.30). Since the diffusion results from purely random procesess in the parallel and perpendicular directions, we can anticipate that this probability distribution will be Gausian and of the form:

$$p(\Delta v_\|, \Delta p) = \frac{1}{2\pi\delta_\|\delta_\perp^2} e^{-\frac{\Delta v_\|^2}{2\delta_\|^2} - \frac{\Delta\Gamma^2}{2\delta_\perp^4}}, \tag{A.31}$$

where

$$\Delta\Gamma = \Delta v^2{}_\perp - \beta\Delta v_\|. \tag{A.32}$$

By requiring

$$< \Delta\Gamma\Delta v_\| >= 0,$$

the average diffusive spreads of the probability distribution are given by

$$\begin{aligned} < \Delta v_\|^2 >&=\delta_\|^2, \\ < (\Delta v_\perp^2)^2 >&=\delta_\perp^4 + \beta^2\delta_\|^2, \\ < \Delta v_\|^2 \Delta v_\perp^2 >&=\beta\delta_\|^2. \end{aligned}$$

From the gyro-averaged collision operator Eq. (A.28), we obtain

$$\delta_\| = \sqrt{\nu_\|(v_\|^2, v) v^2 \Delta t}, \tag{A.33}$$

$$\beta = \frac{\nu_{\|\perp}(v_\|, v_\perp^2)}{\nu_\|(v_\|, v_\perp)} v, \tag{A.34}$$

$$\delta_\perp^2 = v^2 \sqrt{[\nu_\perp(v_\perp^2, v) - \frac{\nu_{\|\perp}^2(v_\|, v_\perp^2)}{\nu_\|(v_\|, v_\perp)}]\Delta t}. \tag{A.35}$$

The Eqs. (A.29)-(A.35) provide a basis for a probablistic numerical approach for the inclusion of Coulomb collisional effects in a gyro-kinetic system. From time saving considerations, we use a square probability amplitude for the random process instead of a Gausian

Eq. (A.31). The diffusive spreads of particle velocity are obtained by computing a random number between -1 and 1 and then multiplying this number by the average diffusive spreads (A.33)-(A.35). Thus we find the new parallel $v'_{\|}$ and perpendicular component $v'^2_{\perp}$ of particle velocity can be evaluated from the old velocities $(v_{\|}, v^2_{\perp}, v)$ by

$$\begin{aligned} v'_{\|} =& v_{\|0}(1-\nu_{s\|}\Delta t) + 2\sqrt{3}(R_{s1}-0.5)\delta_{\|}, \\ v'^2_{\perp} =& v^2_{\perp 0} - v^2\nu_{s\perp}\Delta t + 2\sqrt{3}(R_{s2}-0.5)\delta_{\perp} + 2\sqrt{3}(R_{s1}-0.5)\beta\delta_{\|}, \end{aligned} \qquad (A.36)$$

or

$$\begin{aligned} v'_{\|} =& v_{\|0}(1-\nu_{s\|}\Delta t) + 2\sqrt{3}(R_{s1}-0.5)[\nu_{\|}(v^2_{\|}, v)v^2\Delta t]^{\frac{1}{2}}, \\ v'^2_{\perp} =& v^2_{\perp 0} - v^2\nu_{s\perp}\Delta t + 2\sqrt{3}(R_{s2}-0.5)\{[\nu_{\perp}(v^2_{\perp}, v) - \frac{\nu^2_{\|\perp}(v_{\|}, v^2_{\perp})}{\nu_{\|}(v^2_{\|}, v)}]\Delta t\}^{\frac{1}{2}}v^2 \\ &+ 2\sqrt{3}(R_{s1}-0.5)[\nu_{\|}(v^2_{\|}, v)v^2\Delta t]^{\frac{1}{2}} \cdot \frac{\nu_{\|\perp}(v_{\|}, v^2_{\perp})}{\nu_{\|}(v_{\|}, v^2_{\perp})}v. \end{aligned}$$

ACKNOWLEDGEMENTS

The authors acknowledge their gratitude to Drs. P. H. Diamond, H. Biglari and Y. B. Kim for useful conversations. Our gratitude also goes to Dr. K. H. Burrell and the DIII-D group, and Dr. M. C. Zarnstroff, Dr. Steven Scott, Dr. G. W. Hammett and the TFTR group, for providing us with much valuable data about the ∇T_i-mode and for sharing their physical insights with us. One of us (X. Q. X.) would like to thank P. P. Zhang for her help in preparing the manuscript.

This research was supported by the United States Department of Energy under Contract No. DE-FG05-80ET-53088 with Institute for Fusion Studies, The University of Texas at Austin, and Contract No. DE-FG03-88ER-53275 with University of California, San Diego.

References

1. F. Wagner, G. Becker, K. Behringer, D. Campbell, A. Eberhagen, W. Engelhardt, G. Fussmann, O. Gehre, J. Gernhardt, G. Haas, M. Huang, F. Karger, M. Keilhacker, O. Klüber, M. Kornherr, K. Lackner, G. Lisitano, G. G. Lister, H. H. Mayer, D. Meisel, E. R. Müller, H. M. urmann, H. Niedermeyer, W. Poschenrieder, H. Rapp, H. Röhr, F. Schneider, G. Siller, E. Speth, A. Stäbler, K. H. Steuer, G. Venus, O. Vollmer, and Z. Yü, Phys. Rev. Lett. **49**, 1408(1982).
2. M. Nagami, M. Kasai, A. Kitsunezaki, T. Kobayashi, S. Konoshima, T. Matsuda, N. Miya, H. Ninomiya, S. Sengoku, M. Shimada, H. Yokomizo, T. Angel, C. Armentrout, F. Blau, G. Bramson, N. Brooks, R. Chase, A. Colleraine, E. Fairbanks, J. Fasolo, R. Fisher, R. Groebner, T. Hino, R. Hong, G. Jahns, J. Kamperschroer, J. Kim, A. Lieber, J. Lohr, D. McColl, L. Rottler, R. Seraydarian, R. Silagi, J. Smith, R. Snider, T. Taylor, J. Tooker, D. Vaslow, and S. Wojtowicz, Nucl. Fusion **24**, 183(1984).
3. S. M. Kaye, Phys. Fluids **28**, 2327(1985).
4. K. H. Burrell, S. Ejima, D. P. Schissel, N. H. Brooks, R. W. Callis, T. Carlstrom, A. P. Colleraine, J. C. DeBoo, H. Fukumoto, R. J. Groebner, D. N. Hill, R.-M. Hong, N. Hosogane, G. L. Jackson, G. L. Jahns, G. Janeschitz, A. G. Kellman, J. Kim, L. Lao, P. Lee, J. Lohr, J. L. Luxon, M. Ali Mahdavi, C. P. Moeller, N. Ohyabu, T. H. Osborne, D. Overskei, P. I. Peterson, T. W. Petrie, J. C. Phillips, R. Prater, J. T. Scoville, R. P. Seravdarian, M. Shimada, B. W. Sleaford, R. T. Snider, R. D. Stambaugh, R. D. Stav, H. St. John, R. E. Stockdale, E. J. Strait, T. S. Taylor, J. F. Tooker, and S. Yamaguchi, Phys. Rev. Lett. **59**, 1432(1987).
5. N. Ohyabu, S. Allen, N. H. Brooks, G. Bramson, and K. H. Burrell, General Atomics Rep. GA-A19204(1988).
6. C. Gowers, D. Bartlett, A. Boileau, S. Corti, A. Edwards, N. Gottardi, K. Hirsch, M. Keilhacker, E. Lazzaro, P. Morgan, P. Nielsen, J. O'Rourke, H. Salzmann, P. Smeulders, A. Tanga, and M. von Hellermann, "Profile Behavior During Land H Phases of JET Discharges", in *Proc. of 15th European Conf. on Contr. Fusion and Plasma Heating* (European Physical Society, Dubrovnik, 1988) Vol. 12B, Part 1,

p. 2239.

7. W. M. Tang, G. Rewoldt, and L. Chen, Phys. Fluids **29**, 3715(1986).
8. R. R. Dominguez and R. E. Waltz, Phys. Fluids **31**, 3147(1988). R. R. Dominguez and R. E. Waltz, Nucl. Fusion **29**, 885(1989).
9. F. Romanelli, Phys. Fluids B **1**, 1018(1989). F. Romanelli and S. Briguglio, Phys. Fluids B **2**, 754(1990).
10. H. Biglari, P. H. Diamond, and M. N. Rosenbluth, Phys. Fluids B **1**, 109(1989).
11. R. R. Dominguez and M. N. .Rosenbluth, Nucl. Fusion **29**, 844(1989).
12. T. S. Hahm and W. M. Tang, Princeton Plasma Physics Laboratory Rep. PPPL-2565 (1988).
13. L. Chen, S. Briguglio, and F. Romanelli, submitted to Phys. Fluids B.
14. S. M. Wolfe, Bull. Amer. Phys. Soc. **34**, 1913(1989).
15. M. C. Zarnstorff, N. L. Bretz, P. C. Efthimion, B. Grek, K. Hill, D. Johnson, D. Mansfield,D. McCune, D. K. Owens, H. Park, A. Ramsey, G. L. Schmidt, B. Stratton, E. Synakowski, and G. Taylor, in *Proc. of 16th European Conf. on Contr. Fusion and Plasma Heating*, to be published.
16. F. Romanelli, W. M. Tang, and R. B. White, Nucl. Fusion **26**, 1515(1986).
17. M. Kotschenreuther, Institute for Fusion Studies Report No. 360, "Paticle Simulation With Greatly Reduced Noise".
18. Y. C. Lee and J. W. Van Dam, in *Proceedings of the Finite Beta Theory Workshop*, Varenna, Italy (U. S. Department of Energy, Washington, D. C., 1979), p. 93.
19. J. W. Connor, R. J. Hastie, and J. B. Taylor, Phys. Rev. Lett. **40**, 396(1978); and Proc. R. Soc. London Ser. A**1**, 365(1979).
20. B. B. Kadomtsev and O. P. Pogutse, Zh. Eksp. Teor. Fiz. **51**, 1734(1966) [Sov. Phys.-JETP**24**, 1178(1967)].
21. M. N. Rosenbluth, D. W. Ross, and D. P. Kostomarov, Nucl. Fusion **12**, 3(1972).
22. N. T. Gladd and D. W. Ross, Phys. Fluids **16**, 1706(1973).
23. W. M. Tang, J. C. Adam, and D. W. Ross, Phys. Fluids **20**, 430(1977).
24. M. Tagger, G. Laval, and R. Pellat, Nucl. Fusion **17**, 109(1977).
25. R. Marchand, W. M. Tang, and G. Rewoldt, Phys. Fluids **23**, 1164(1980).

26. H. Biglari, P. H. Diamond, and P. W. Terry, Phys. Rev. Lett. **60**, 200(1988).
27. X. Q. Xu and M. N. Rosenbluth, to be published.
28. T. M. Antonsen and B. Lane, Phys. Fluids **23**, 1205(1980).
29. P. J. Catto, W. M. Tang, and D. E. Baldwin, Plasma Phys. **23**, 639(1981).
30. C. K. Birdsall and A. B. Langdon, **Plasma Physics via Computer Simulation**, (McGraw-Hill, New York, 1985).
31. G. Rewoldt, W. M. Tang, and M. S. Chance, Phys. Fluids **25**, 480(1982). G. Rewoldt, W. M. Tang, and R. J. Hastie, Phys. Fluids **30**, 807(1987).
32. W. W. Lee and W. M. Tang, Phys. Fluids **31**, 612(1988).
33. R. D. Sydora, Bull. Amer. Phys. Soc. **34**, 2138(1989).
34. M. Kotschenreuther, Bull. Amer. Phys. Soc. **33**, 2107(1988).
35. H. V. Wong and P. Lyster, Bull. Amer. Phys. Soc. **34**, 2045(1989).
36. Ejima and Doublet III group, Nucl. Fusion **22**, 1627(1982).
37. M. Greenwald, D. Gwinn, S. Milora, J. Parker, R. Parker, and S. Wolfe, *10th International Conference on Plasma Physics and Controlled Nuclear Fusion Research*, London (IAEA, Vienna, 1984) Vol. 1, p. 45.
38. M. N. Rosenbluth, W. M. Macdonald, and D. L. Judd, Phys. Rev. **1**, 107(1957).
39. P. J. Catto and K. T. Tsang, Phys. Fluids **20**, 396(1977).
40. J. Q. Dong, P. N. Guzdar, and Y. C. Lee, Phys. Fluids **30**, 2694(1987).
41. G. Rewoldt and W. M. Tang, Phys. Fluids B**2**, 318(1990).
42. B. G. Hong, W. Horton and D.-I. Choi, Plasma Phys. and Contr. Fusion **31**, 1291(1989).
43. G. S. Lee and P. H. Diamond, Phys. Fluids **29**, 3291(1986).
44. S. Hamaguchi and W. Horton, IFSR #383, to appear in Phys. Fluids B; S. Hamaguchi and W. Horton, IFSR #430, to appear in Phys. Fluids B.

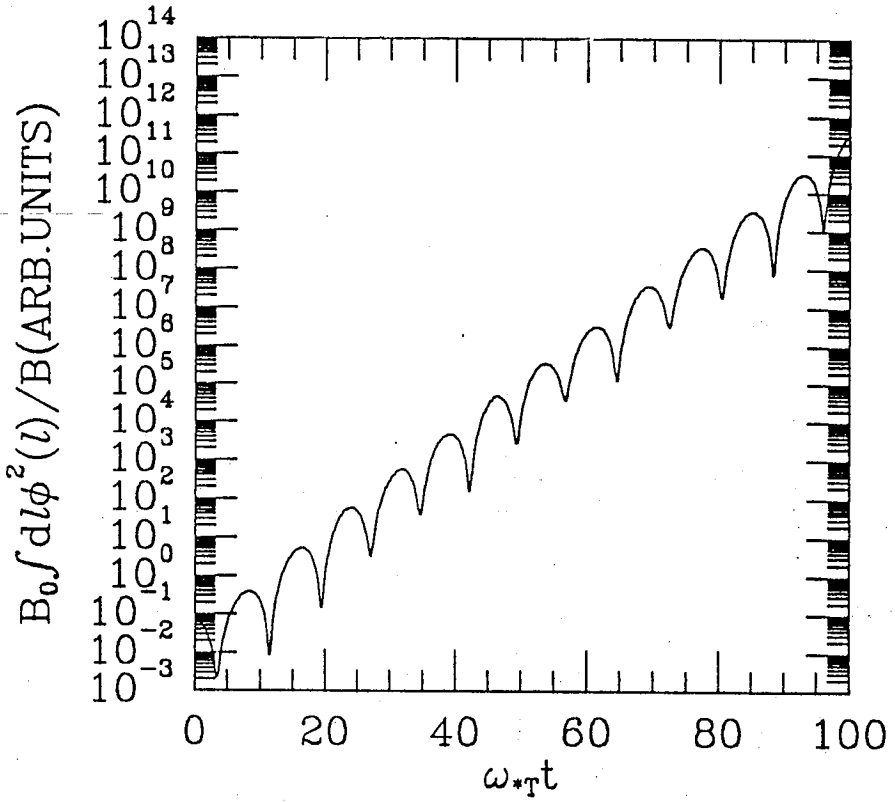

Fig. 1. Total potential energy of the system $\int dl\phi^2(l)$ vs time $\omega_{*T}t$ in toroidal model for $\eta_i = \infty$, $\hat{s} = \tau = 1.0$, $k_\chi \rho_s = 0.4$, $\nu_i^* = 0.0$, and $L_{Ti}/R_0 = 0.1$. The eigenfrequency is $\omega/\omega_{*T} = -0.41 + i0.144$.

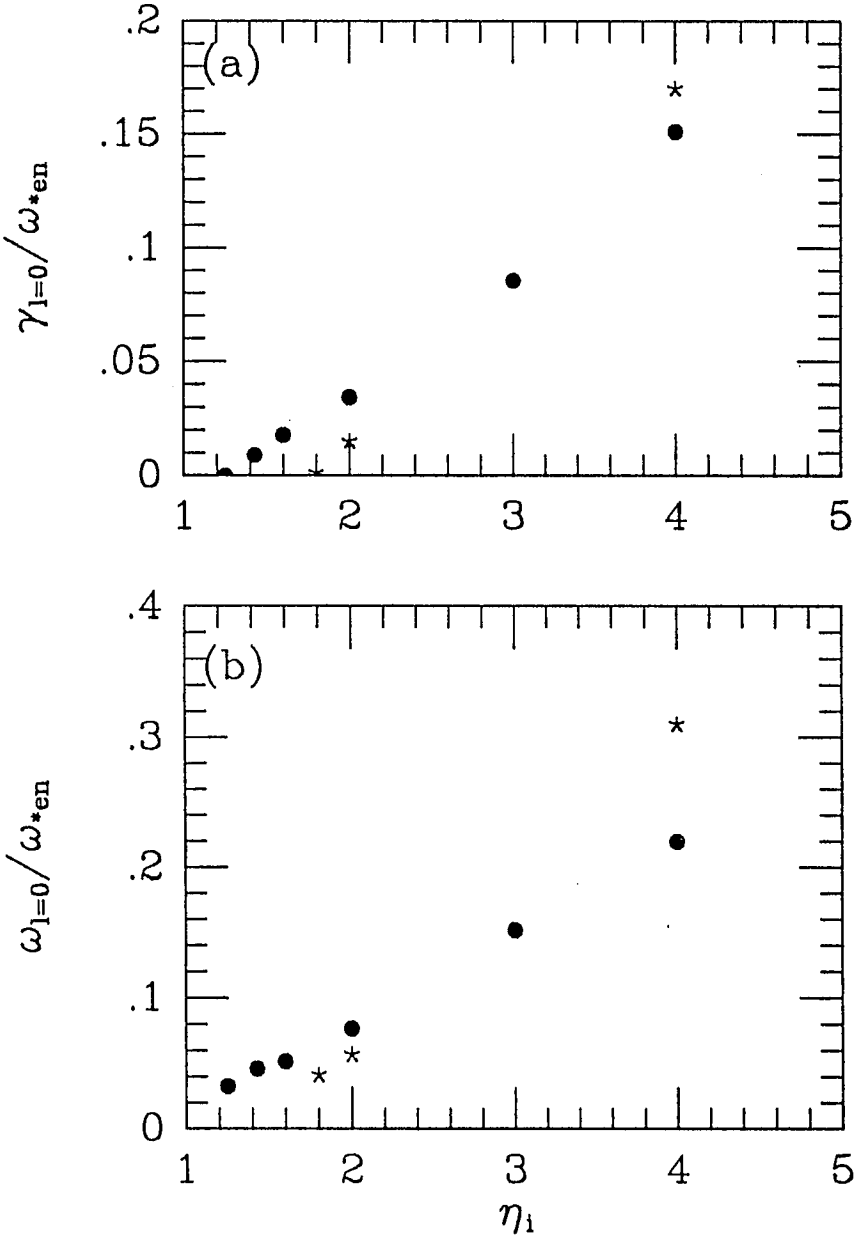

Fig. 2. Growth rate (a) and real part of frequency (b) versus η_i in slab model for $L_s/\rho_s = 200.0$, $L_s/L_n = 5.0$, $k_y\rho_s = 0.2$, and $\tau = 1.0$.

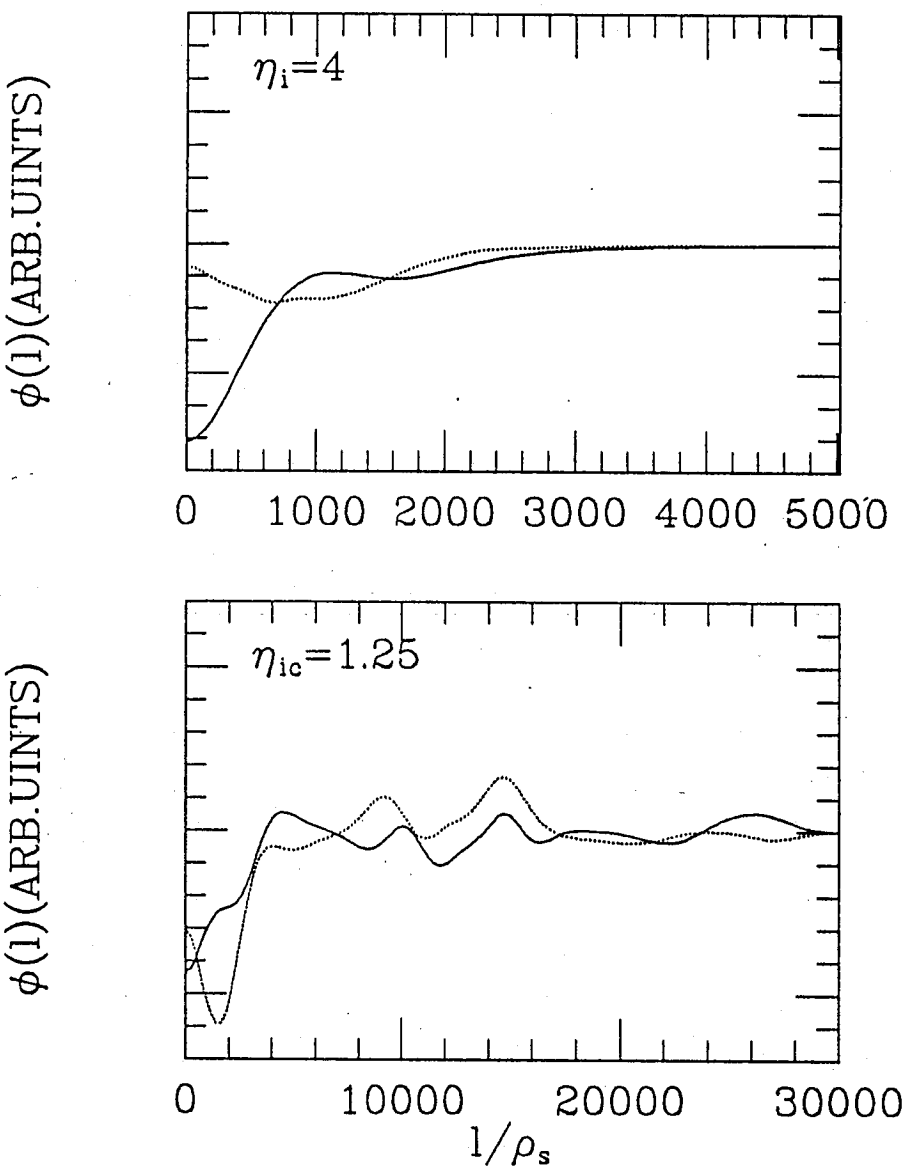

Fig. 3. Real (solid line) and imaginary (dotted line) part of the eigenfunction $\phi(l)$ in slab model for $k_y\rho_s = 0.2$, $L_s/\rho_s = 200.0$, $L_s/L_n = 5.0$, and $\tau = 1.0$. (The phase of the eigenfunction at l=0 is arbitrary).

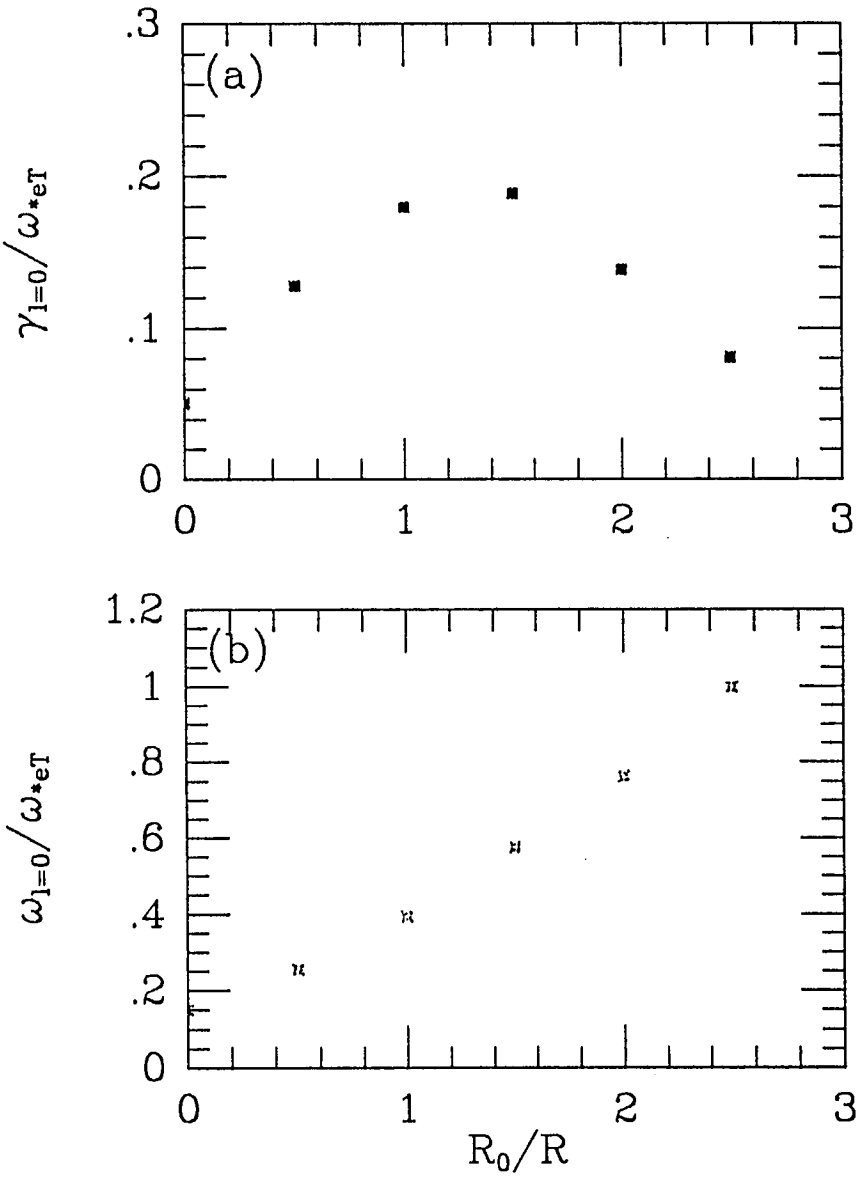

Fig. 4. Growth rate (a) and real part of frequency (b) versus R_0/R for $k_\chi \rho_s = 0.1$, and $\hat{s} = \tau = 1.0$. R is the theoretical major radius and R_0 the DIII-D major radius. During the transition ($R = \infty \rightarrow 0.4R_0$), L_{Ti}, L_s and r_0 are fixed, where r_0 is the radial position of $q(r_0) = 2$ rational surface. But $\omega_d/\omega_{*T} = L_{Ti}/R = 0.1R_0/R$ and $\epsilon = r_0/R = 0.3R_0/R$ are varied versus R_0/R.

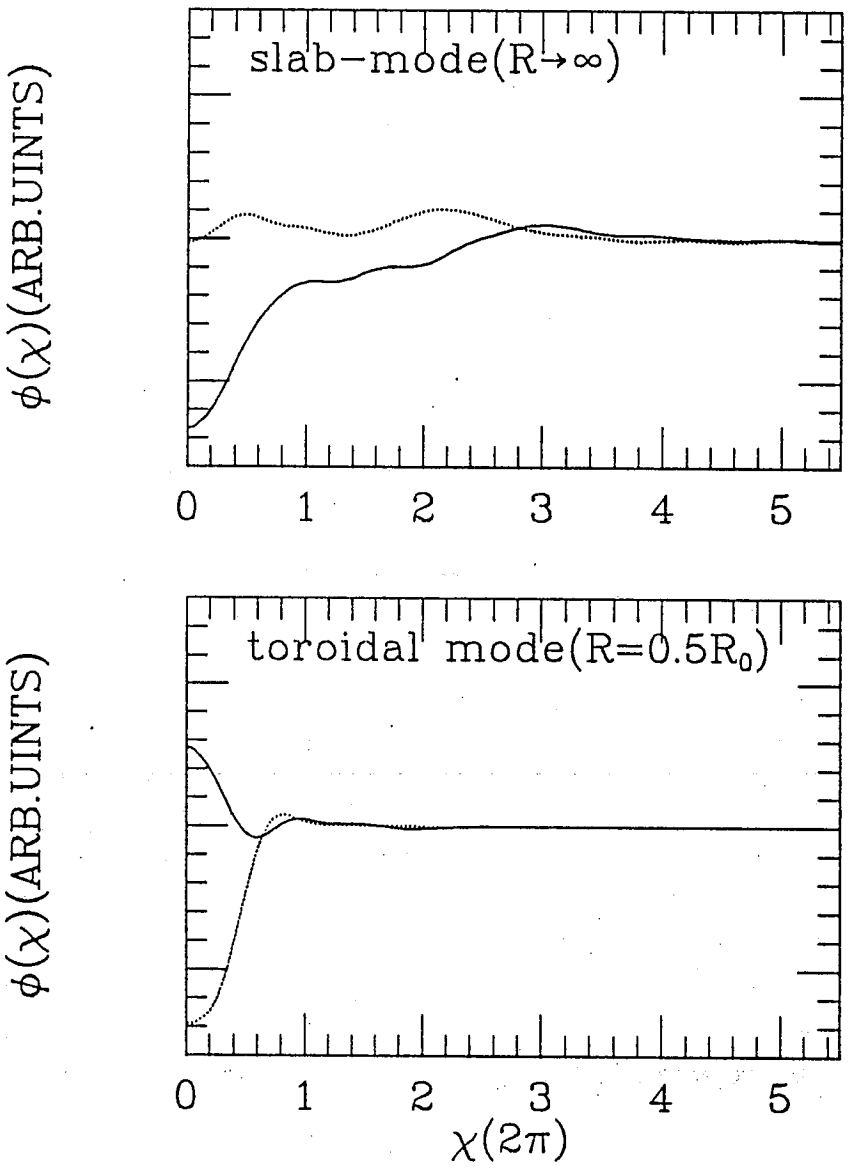

Fig. 5. Real (solid line) and imaginary (dotted line) part of the eigenfunction $\phi(\chi)$ in slab model (above) and in toroidal model (below) for the same parameters and mode as in Fig. 4. (The phase of the eigenfunction at χ=0 is arbitrary).

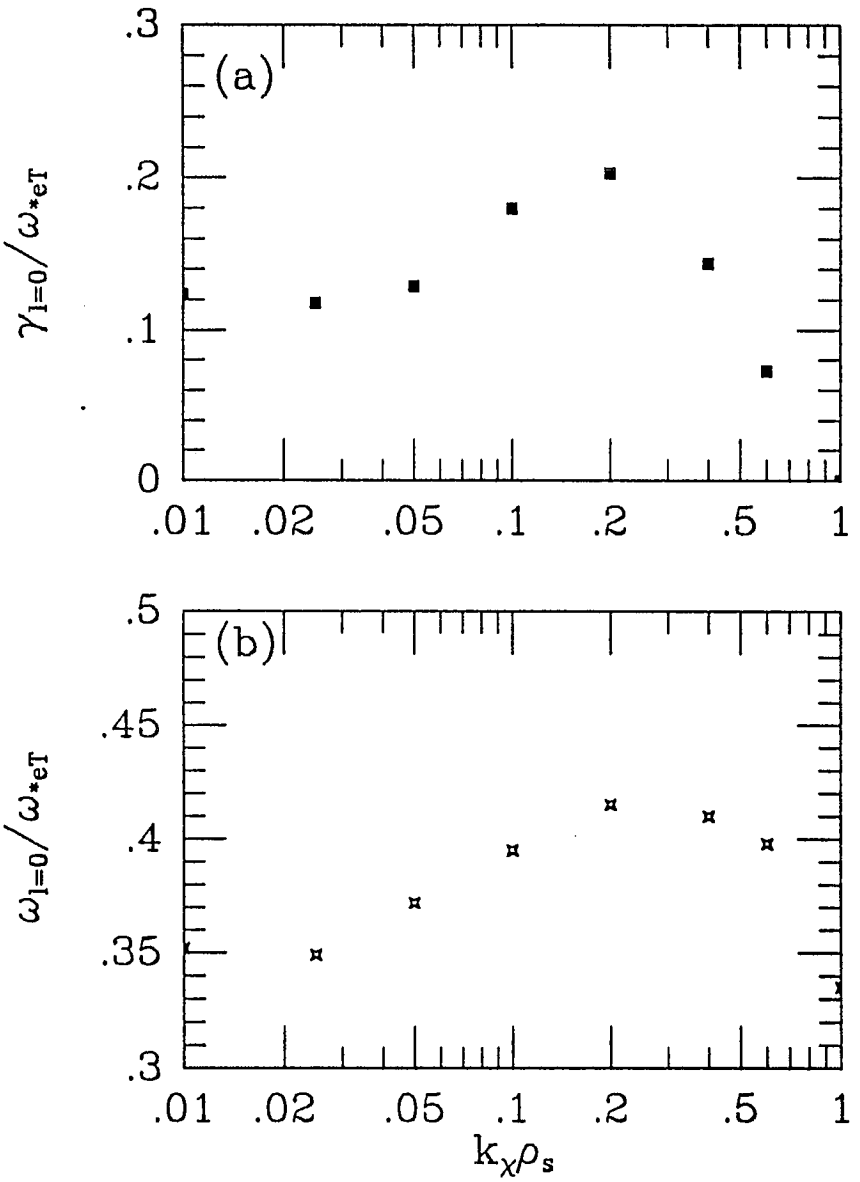

Fig. 6. Growth rate (a) and real part of frequency (b) versus $k_\chi \rho_s$ for $L_{Ti}/R_0 = 0.1$, $\nu_i^* = 0.0$ and $\hat{s} = \tau = 1.0$.

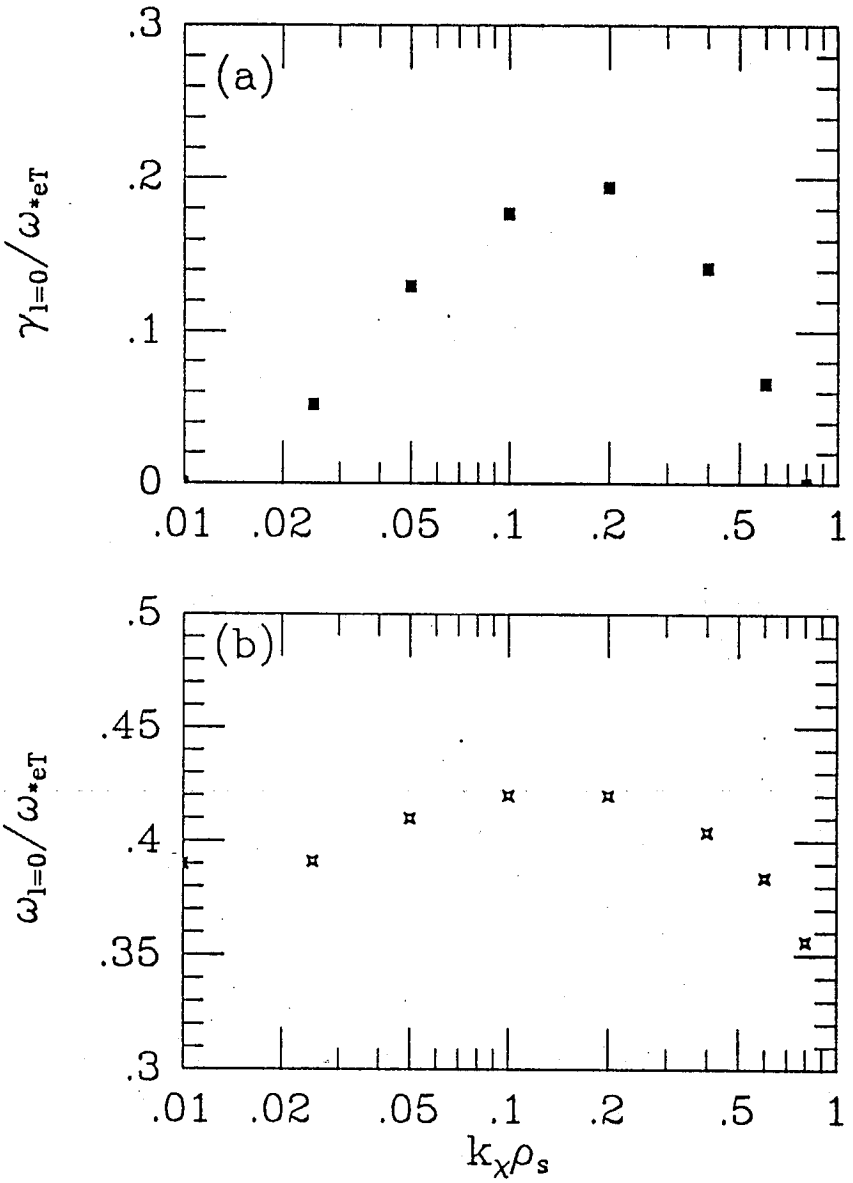

Fig. 7. Growth rate (a) and real part of frequency (b) versus $k_\chi \rho_s$ for $L_{Ti}/R_0 = 0.1$, $\nu_i^* = 1.02$ and $\hat{s} = \tau = 1.0$.

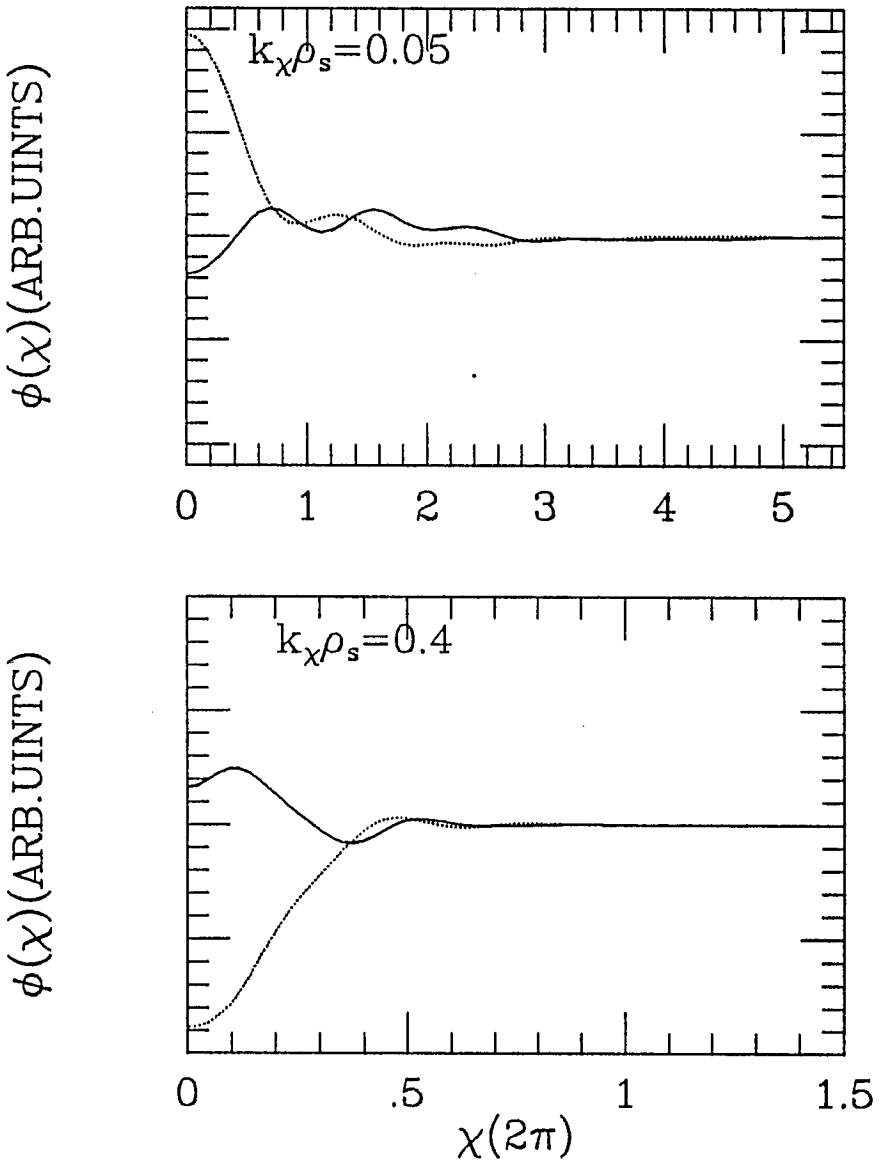

Fig. 8. Real (solid line) and imaginary (dotted line) part of the eigenfunction $\phi(\chi)$ for parameters: $L_{Ti}/R_0 = 0.1$, $\nu_i^* = 0.0$, and $\hat{s} = \tau = 1.0$. (The phase of the eigenfunction at χ=0 is arbitrary).

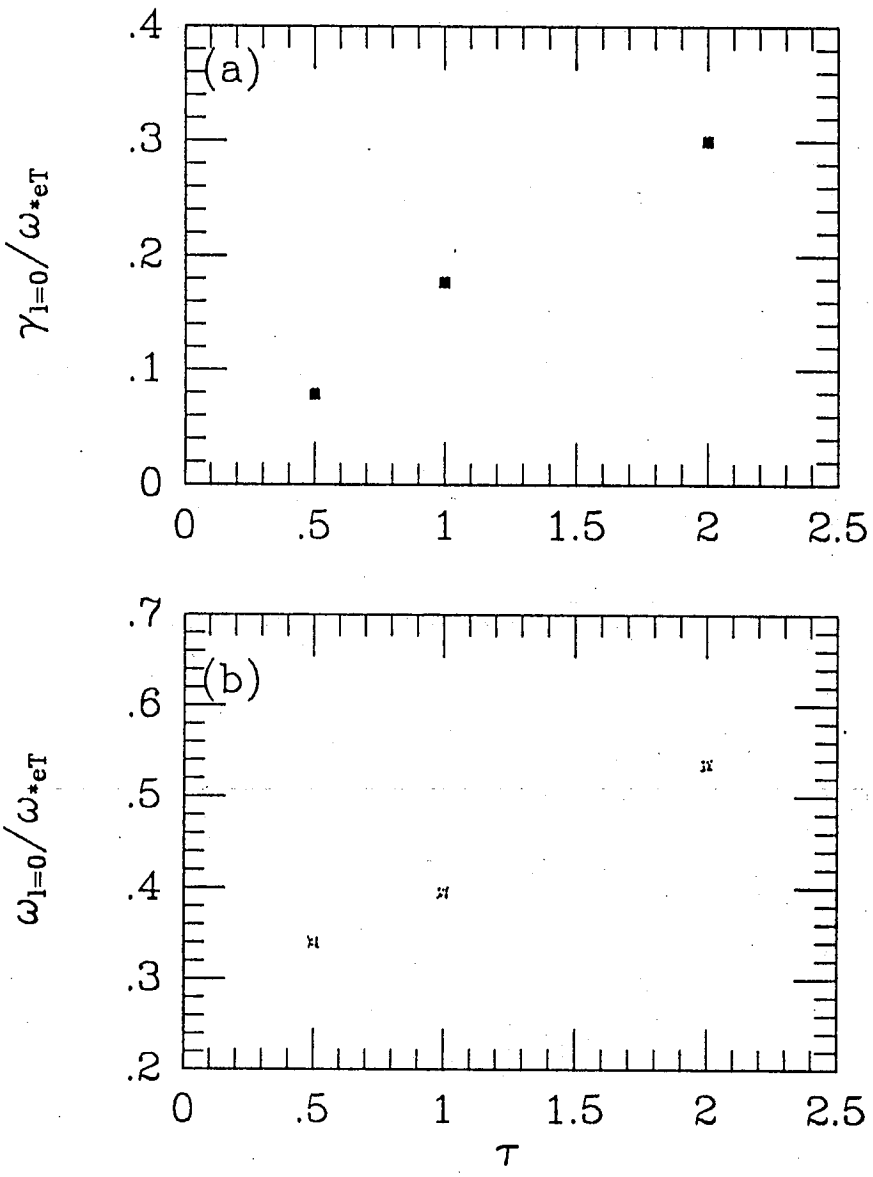

Fig. 9. Growth rate (a) and real part of frequency (b) versus τ for $L_{Ti}/R_0 = 0.1$, $k_\chi \rho_s = 0.1$, $\nu_i^* = 0.0$, and $\hat{s} = 1.0$.

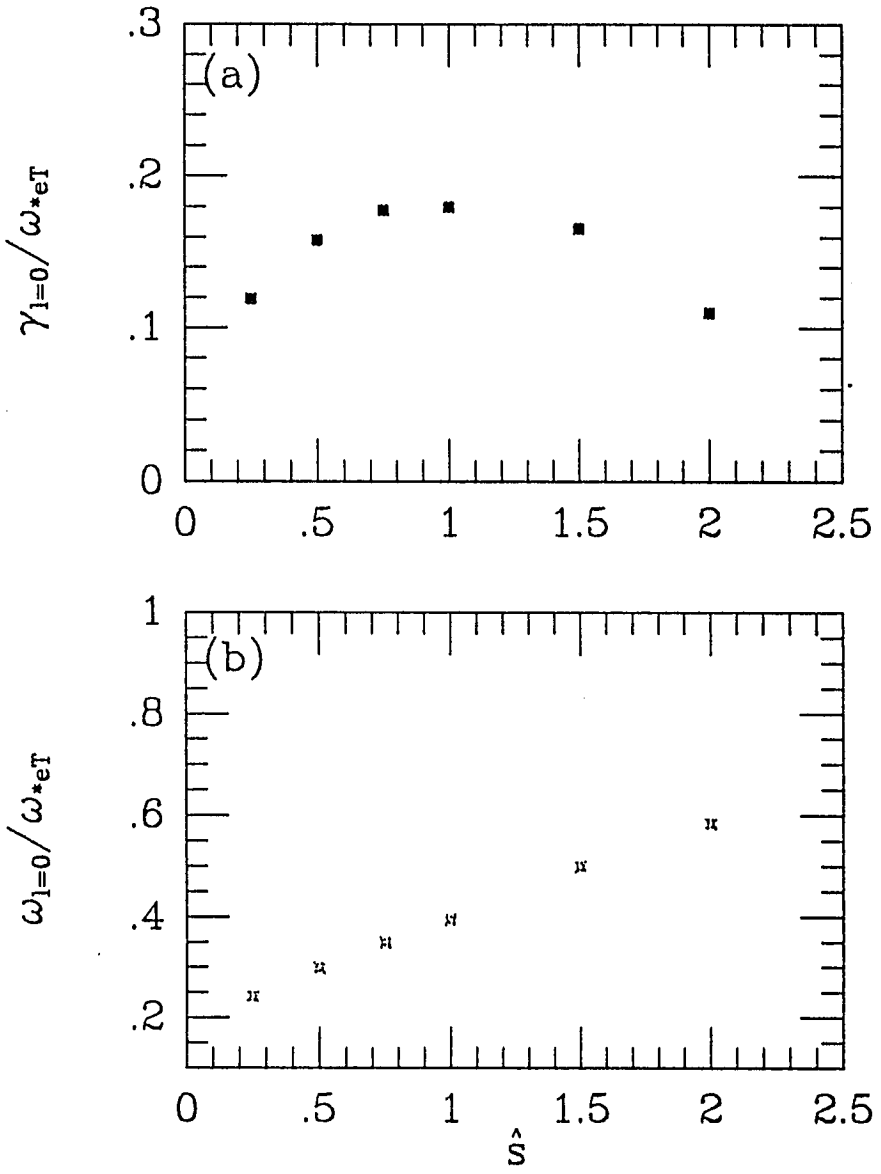

Fig. 10. Growth rate (a) and real part of frequency (b) versus $\hat{s}$ for $L_{Ti}/R_0 = 0.1$, $k_\chi \rho_s = 0.1$, $\nu_i^* = 0.0$, and $\tau = 1.0$.

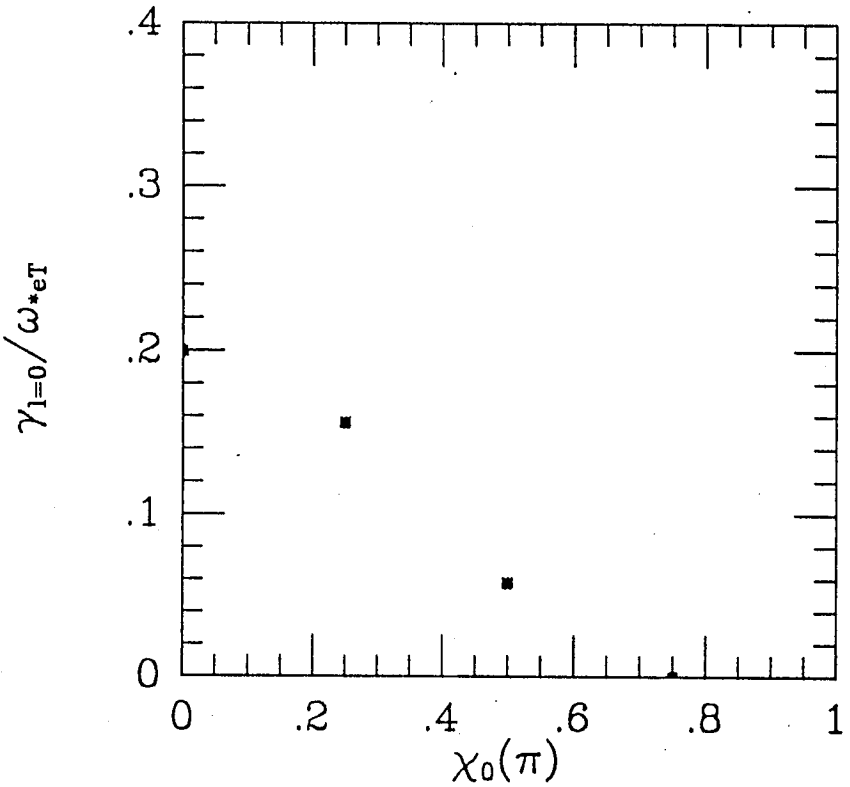

Fig. 11. Growth rate versus χ_0 for $L_{Ti}/R_0 = 0.1$, $k_\chi \rho_s = 0.1$, $\nu_i^* = 0.0$, and $\hat{s} = \tau = 1.0$.

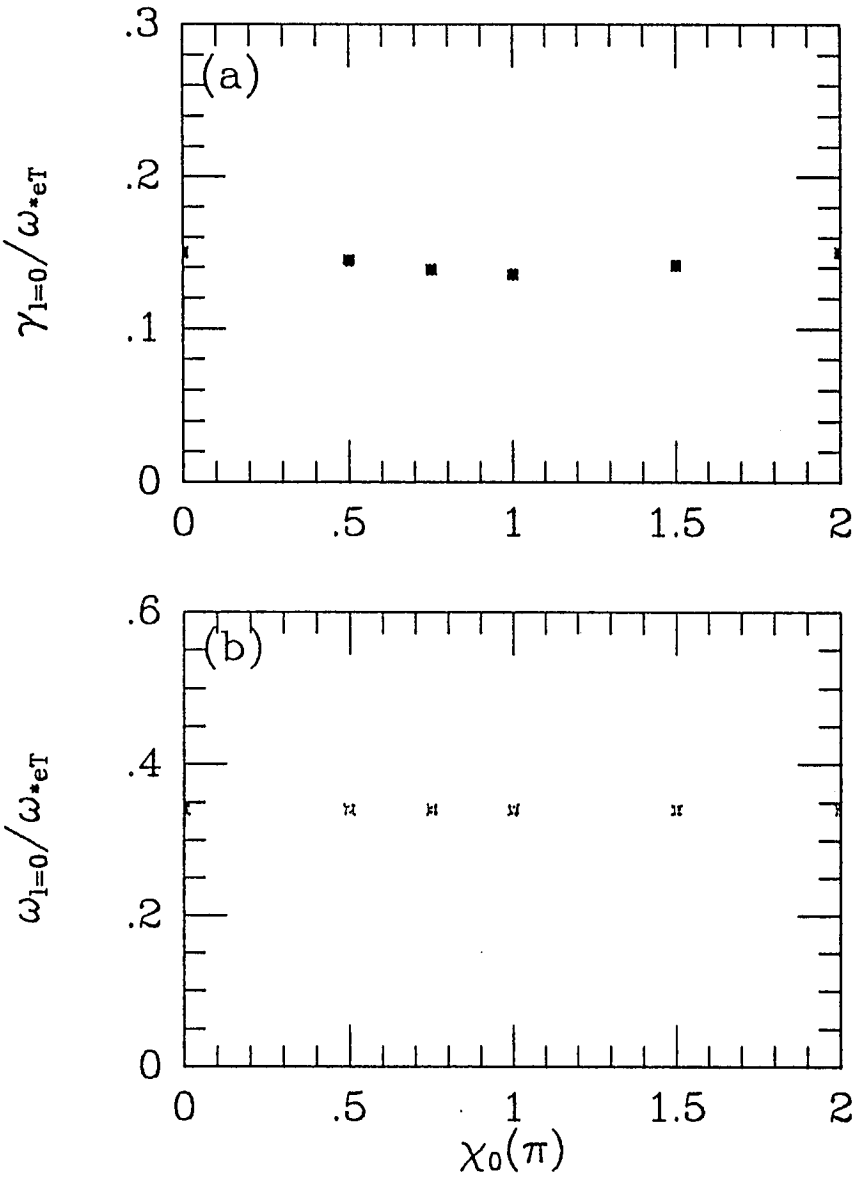

Fig. 12. Growth rate (a) and real part of frequency (b) versus χ_0 for $L_{Ti}/R_0 = 0.1$, $k_\chi \rho_s = 0.025$, $\nu_i^* = 0.0$, and $\hat{s} = \tau = 1.0$.

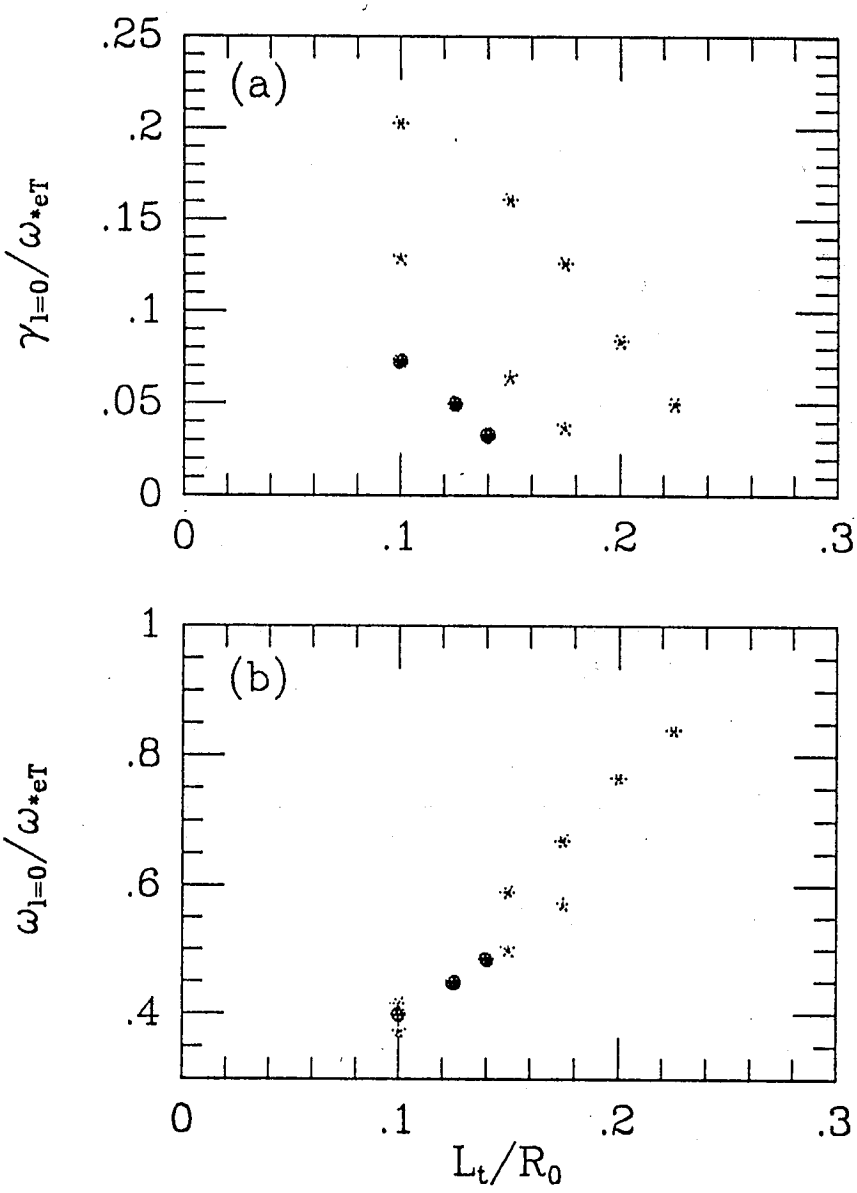

Fig. 13. Growth rate (a) and real part of frequency (b) versus L_{Ti}/R_0 for $\nu_i^* = 0.0$, $\hat{s} = \tau = 1.0$, and following parameters: $*$ $k_\chi \rho_s = 0.2$, $\star$ $k_\chi \rho_s = 0.05$, and $\bullet$ $k_\chi \rho_s = 0.6$.

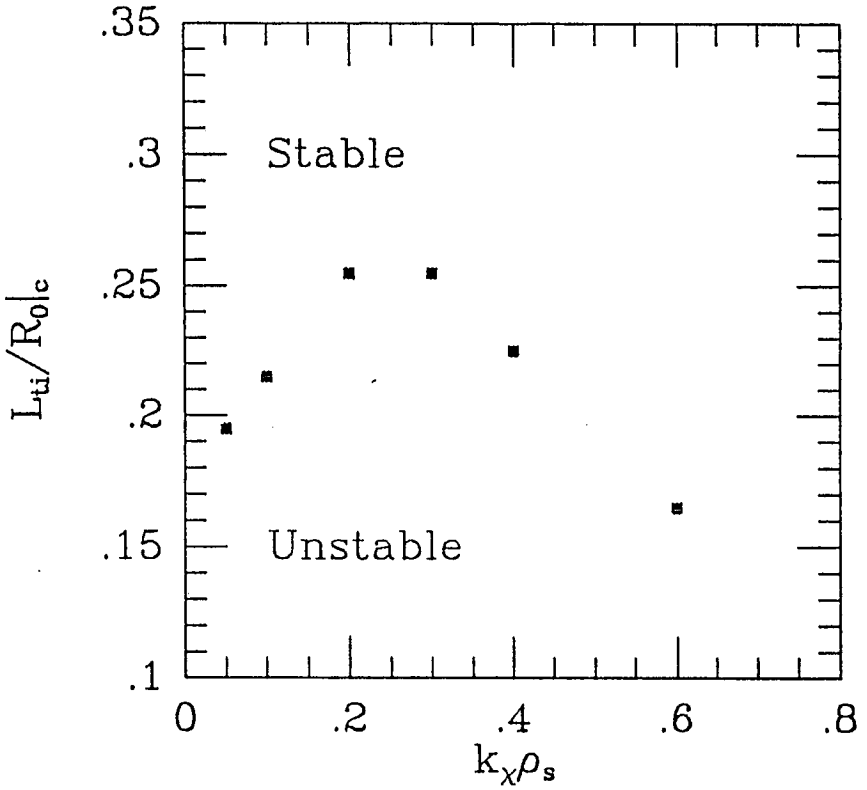

Fig. 14. Stable and unstable regions in L_{Ti}/R_0 vs $k_\chi \rho_s$ for $\nu_i^* = 0.0$ and $\hat{s} = \tau = 1.0$.

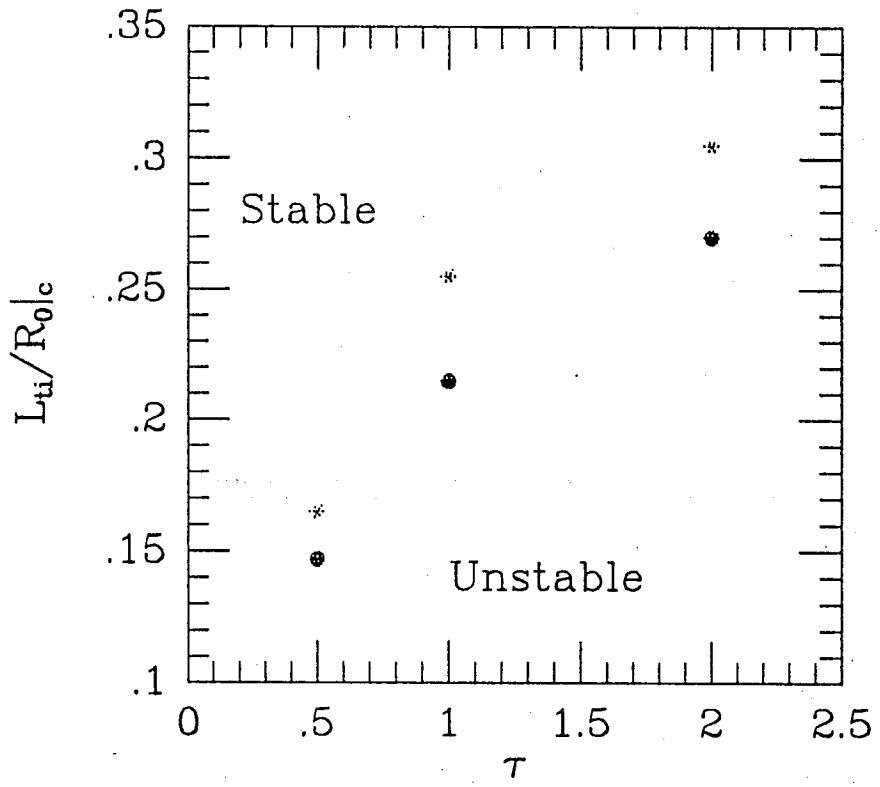

Fig. 15. Stable and unstable regions in L_{Ti}/R_0 vs τ for $\nu_i^* = 0.0$, $\hat{s} = 1.0$, • $k_\chi \rho_s = 0.1$ and $*$ $k_\chi \rho_s = 0.2$.

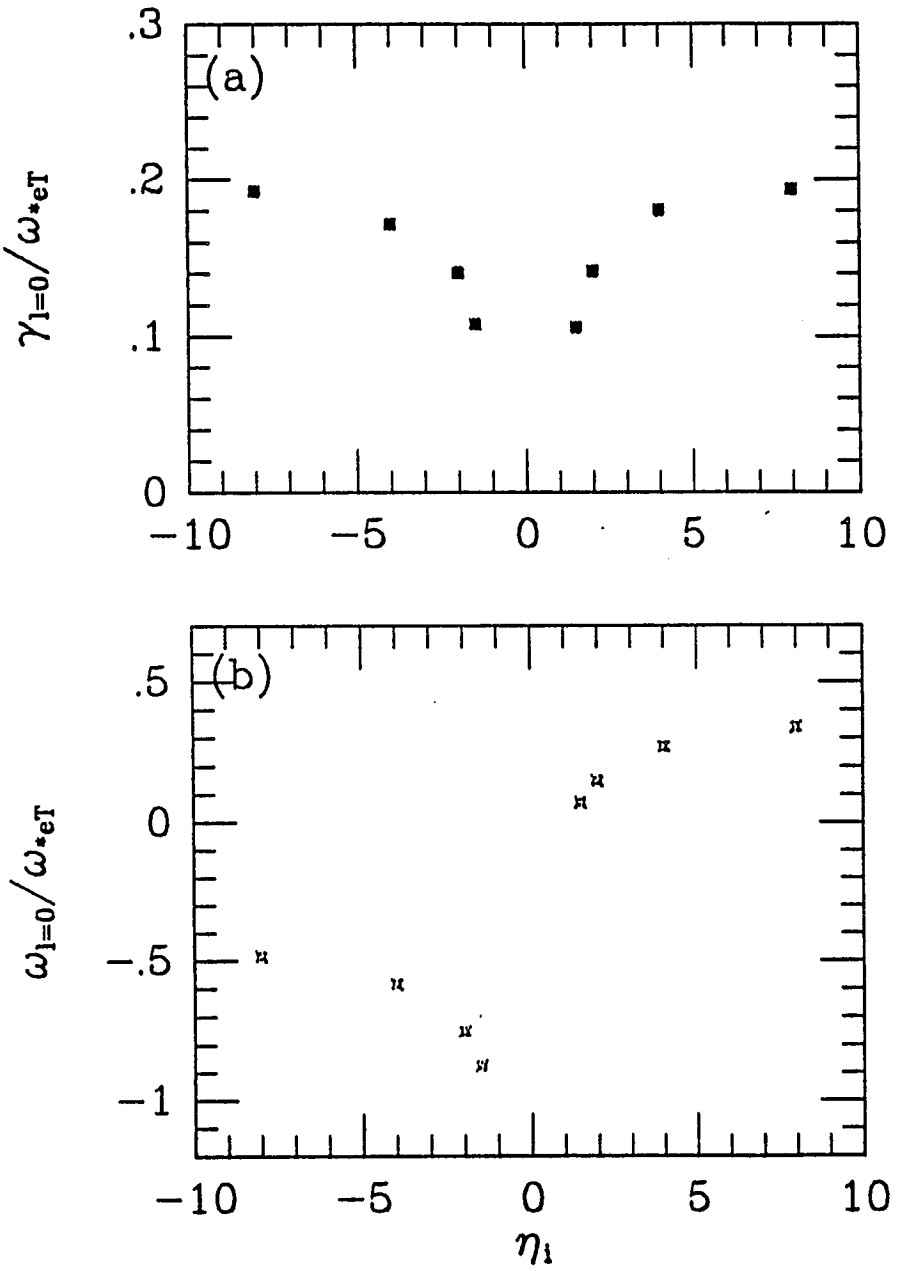

Fig. 16. Growth rate (a) and real part of frequency (b) versus η_i for $L_{Ti}/R_0 = 0.1$, $k_\chi \rho_s = 0.1$, $\nu_i^* = 0.0$, and $\hat{s} = \tau = 1.0$.

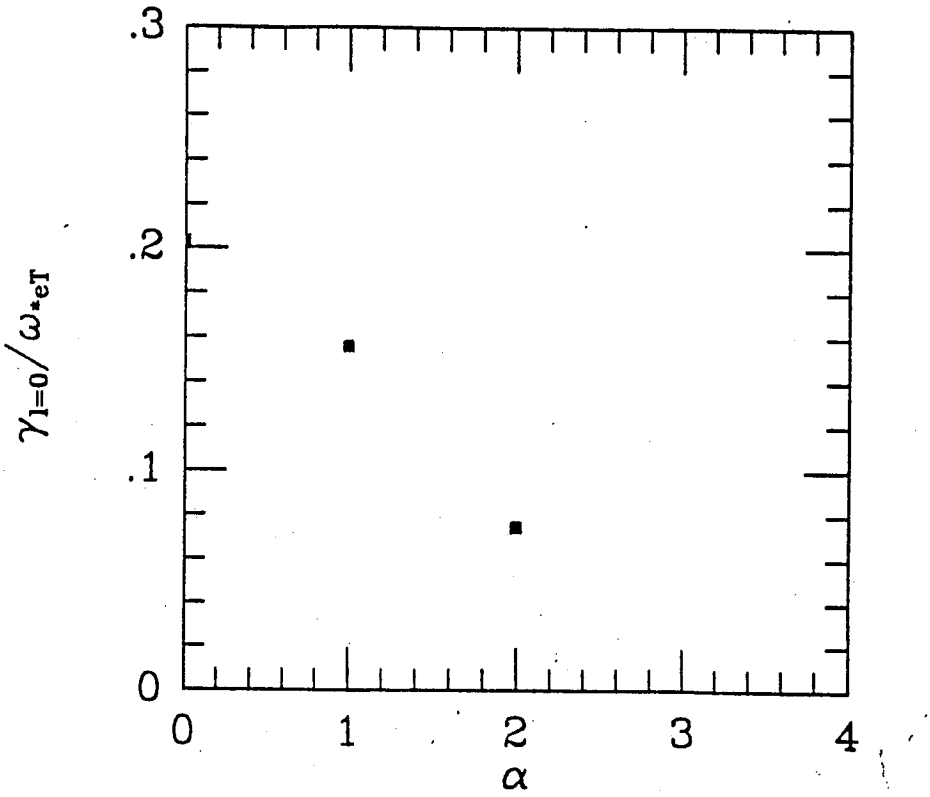

Fig. 17. Growth rate versus α for $\eta_i = \infty$, $L_{Ti}/R_0 = 0.1$, $k_\chi \rho_s = 0.2$, $\nu_i^* = 0.0$, and $\hat{s} = \tau = 1.0$.